

THESIS

EXTREME ULTRAVIOLET TIME-OF-FLIGHT MASS SPECTROMETRY FOR THE
CHARACTERIZATION OF ACTINIDES

Submitted by

Tyler Green

Department of Electrical and Computer Engineering

In partial fulfillment of the requirements

For the Degree of Master of Science

Colorado State University

Fort Collins, Colorado

Summer 2017

Master's Committee:

Advisor: Carmen Menoni

Dean Crick

Mario Marconi

Copyright by Tyler Green 2017

All Rights Reserved

ABSTRACT

EXTREME ULTRAVIOLET TIME-OF-FLIGHT MASS SPECTROMETRY FOR THE CHARACTERIZATION OF ACTINIDES

Many scientific disciplines, as well as several technologies, have a great demand for analytical tools capable of assessing chemical composition and imaging chemical content that are highly sensitive and have sub-micron spatial resolution. Laser ablation mass spectrometry meets both of these requirements and as such is broadly used for chemical analyses and chemical mapping of atomic and molecular species on solid samples.

This thesis describes results on the characterization of Extreme Ultraviolet Time-of-Flight Laser Ablation Mass Spectrometry (EUV TOF) for analysis of trace actinides and for high lateral resolution imaging of inorganic samples. We demonstrate that this technique, with a nominal sensitivity around 50 ppm and a lateral resolution of 80 nm, is already competitive with other well-established mass spectrometry techniques that focus on analytical isotopic imaging. The thesis also details the diagnosis and determination of causes of noise that compromise sensitivity in the mass spectra. These results enable EUV TOF to properly orient itself in the field of mass spectrometry and allow multiple disciplines to conduct high resolution compositional mapping quickly and with minimal isobaric interferences.

ACKNOWLEDGEMENTS

First and foremost I would like to thank Dr. Carmen Menoni for all of the support and guidance she has given me over the past 3 years. She has always been a wellspring of enthusiasm for the work involving EUV TOF, and I admire her welcoming demeanor to all new students who enter the ERC.

I owe very much to Ilya Kuznetsov who taught me all about the EUV TOF system when I first arrived, introduced me to machining, and must have answered at least hundreds of questions from me over the past few years.

Most of this work would not have been possible without Pacific Northwest National Laboratory (PNNL) and the collaboration and support of Dr. Andrew Duffin. I would also like to thank Dr. Dean Crick and Dr. Mario Marconi for serving on my committee.

Lastly I would like to thank my family for the support they have given me throughout my life. Their constant love and encouragement, especially when the road gets rough, has enabled me to succeed, and I am very lucky for it.

TABLE OF CONTENTS

Abstract.....	ii
Acknowledgements.....	iii
Chapter 1: Basics of Inorganic Mass Spectrometry.....	1
1.1 Introduction to Mass Spectrometry.....	1
1.2 Laser Based Mass Spectrometry.....	5
1.3 Secondary Ion Mass Spectrometry: TOF SIMS and Dynamic SIMS.....	7
1.4 EUV Mass Spectrometry.....	9
1.5 NIST Calibration Glasses.....	11
1.6 Nuclear Forensics.....	12
1.7 Overview of the Thesis.....	14
Chapter 2: Description of the EUV TOF Mass Spectrometry System.....	17
2.1 Overview of the system.....	17
2.2 Details of the System.....	19
2.3 Samples Used in Analysis.....	29
Chapter 3: Noise Source Identification and Mitigation.....	33
3.1 Noise Identification.....	33
3.2 Noise Mitigation.....	47
Chapter 4: Mass Spectrometry Analysis and Imaging of Trace Elements and Actinides.....	49
4.1 Introduction.....	49
4.2 Trace Analysis.....	50

4.3 Sample Utilization Efficiency.....	56
4.4 Lateral Resolution.....	58
4.5 Uranium Oxide Particle Imaging.....	60
Chapter 5: Conclusions and Future Work.....	63
5.1 Need for sensitive mass spectrometry systems.....	63
5.2 Conclusion and Results.....	63
5.3 Future Work.....	64
Bibliography.....	65

Chapter 1: Basics of Inorganic Mass Spectrometry

1.1 Introduction to Mass Spectrometry

Mass spectrometry is an analytical technique with the capability to assess the composition of a sample on an atomic and molecular level. This technique has proven to be a very useful analytical tool across multiple scientific disciplines and in technology. Mass spectrometers can analyze gaseous and solid samples. With the latter, mass spectrometers can be used to map chemical composition, which has proven to be important in biological applications.

A mass spectrometer is composed of an ion source, a mass analyzer, and a detector¹ as schematically shown in Fig. 1. The source creates ions and neutral atoms and molecules. The ions are extracted into the mass analyzer which discriminates the ions by their mass vs charge ratio. Finally, the detector detects the ions and converts them into a current signal. There is a large family of mass spectrometers, each with unique characteristics tailored to analyze gas, liquid, and solid samples. In the analysis of solid samples, laser ablation inductively-coupled plasma mass spectrometry (LA-ICP-MS) and secondary ion mass spectrometry are broadly used²⁻⁴.

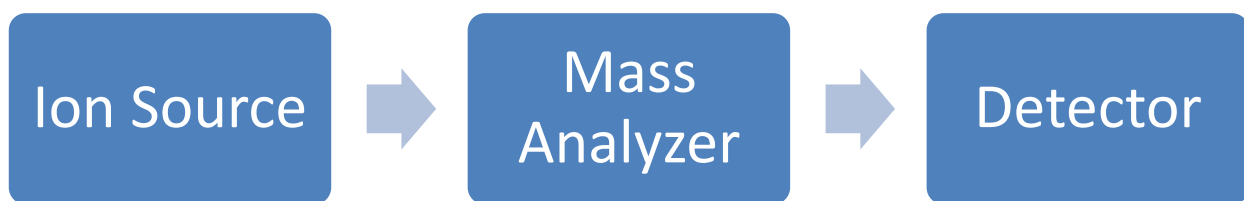


Fig.1: Flow chart describing the creation of ions, their separation in a mass analyzer, and then detection.

There are different types of mass analyzers, such as Time-of-Flight, Inductively-Coupled Plasma, Magnetic Sector, Quadrupole, and others. Some of the more common mass analyzers will be described in this section. A Time-of-Flight (TOF) mass analyzer is usually used with a pulsed source that produces a packet of ions to extract for imaging applications^{5,6}. TOF is typically used when excellent temporal resolution is needed or to gain access to a large mass range. A schematic of a TOF system is shown in Figure 2. It works by accelerating ions using voltage grids and having the ions separate out by their time of flight. Since each ion is being affected by the same electric field, E, and travel the same distance, z, in the extraction region, they each gain a potential energy equal to:

$$U = zEx = zV \quad (1-1)$$

where V is the electric potential.

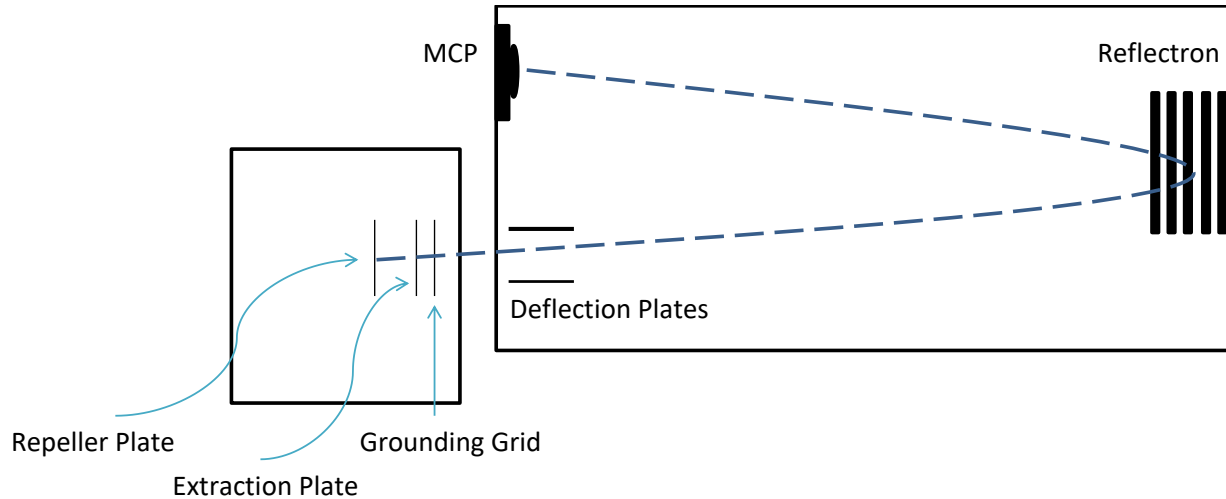


Fig. 2: Diagram showing a top down view of a Time-of-Flight chamber including a reflectron⁷ which reflects the ions in the chamber. The dotted-blue line represents the path ions take from the ionization chamber to the detector.

The positive ions are accelerated in the constant electric field E until they reach a grounding grid in which their potential energy turns into kinetic energy, which equals to:

$$E = \frac{1}{2}mv^2 \quad (1-2)$$

where v is the ion velocity. By combining equations 2 and 3 together:

$$\frac{m}{z} = \frac{2V}{v^2} \quad (1-3)$$

Equation 1-3 shows that lighter mass ions have a higher velocity than heavier mass ions with the same charge. With a simple substitution where,

$$v = \frac{L}{t} \quad (1-4)$$

with L being the drift length the ions travel we get:

$$t = \sqrt{\frac{m}{2zV}} * L \quad (1-5)$$

Equation 1-5 shows that heavier mass ions arrive at the detector at a later time than lighter ions with the same charge. These ions collide with the detector one after the other in roughly the same location. Commonly these systems incorporate an ion lens that minimizes the amount the ions drift laterally from one another, and a reflectron can be used to correct for any difference in initial kinetic energy between ions of the same mass^{8,9}. By knowing the distance the ions travel, one can correlate the ions' time of arrival with the mass versus charge (m/z) of the particle. The major benefit of a TOF is the ability to collect an entire mass spectrum from a location on a sample without needing to preselect a m/z value to observe. This makes it an excellent method for mapping the composition of compounds on a sample with high throughput and is the most commonly used method for pulsed source techniques¹⁰. The

limitations of a TOF are its limited dynamic range and sensitivity compared to other techniques¹¹.

Another example of a mass analyzer is a magnetic sector, schematically shown in Figure 3¹². This is the oldest detection method of mass spectrometry and it works by accelerating ions into a magnetic field and separating them laterally using the magnetic field contribution of the Lorentz force:

$$F = z(v \times B) \quad (1-6)$$

This technique places strong ~1 Tesla magnets, orthogonal to the direction of ion travel so the above equation simplifies to:

$$F = zvB \quad (1-7)$$

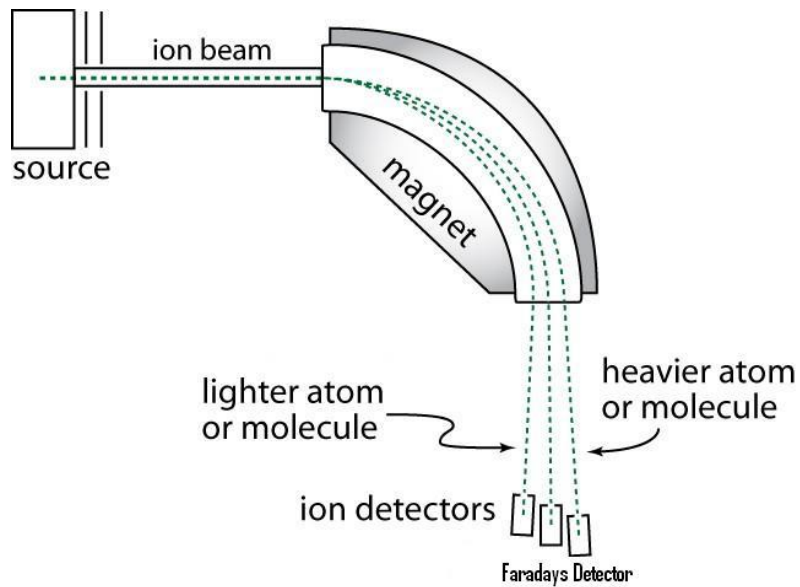


Fig 3: Top down diagram of a magnetic sector instrument. The ions are represented using green, dashed lines.

This Lorentz force acting on the ions is a centripetal force that causes the ions to travel in an arc whose radius is dictated by the ion's mass:

$$F_L = zvB = F_C = \frac{mv^2}{r} \quad (1-8)$$

By rearranging the terms and substituting the elementary charge e with the broader charge z :

$$\frac{m}{z} = \frac{B}{vr} \quad (1-9)$$

where the initial velocity is determined by the voltages set on the extraction optics.

In these systems, a slit is placed just before the detector so that only a specific mass is detected. The benefits of this system, in contrast to the TOF, are high mass resolution and high sensitivity. This type of system can be used for isotopic ratio analysis and trace analysis using continuous sources. The limitations of this system are that it can only measure a limited mass window.

1.2 Laser Ablation Mass Spectrometry

Laser ablation, coupled with mass spectrometers, are very useful in determining the composition of solid samples. In particular this method is useful in determining the composition of glasses due to the speed of analysis and the spatial resolution that can be achieved. Almost all of the research done using lasers in inorganic mass analysis of solids have been performed using Laser Ablation Inductively Coupled Plasma Mass Spectrometry (LA-ICP-MS)^{13–19}. This is because almost every laser-based mass spectrometry system uses a laser with photons energetic enough to cause ablation in solids. A common laser used in LA-ICP-MS is Nd:YAG or Nd:YLF, either used at their fundamental wavelength around 1000 nm, or upconverted down to as low as ~200 nm wavelength using their fourth or fifth harmonic^{14–16,20}. With a maximum of

\sim 6eV photon energy, these systems require an ICP to ionize most ablated particles. Depending on the laser pulse duration, whether in the nano-, pico-, or femtosecond regime, ablation mechanisms can differ. Figure 4 shows craters and lines ablated with nano- and femtosecond lasers²¹.

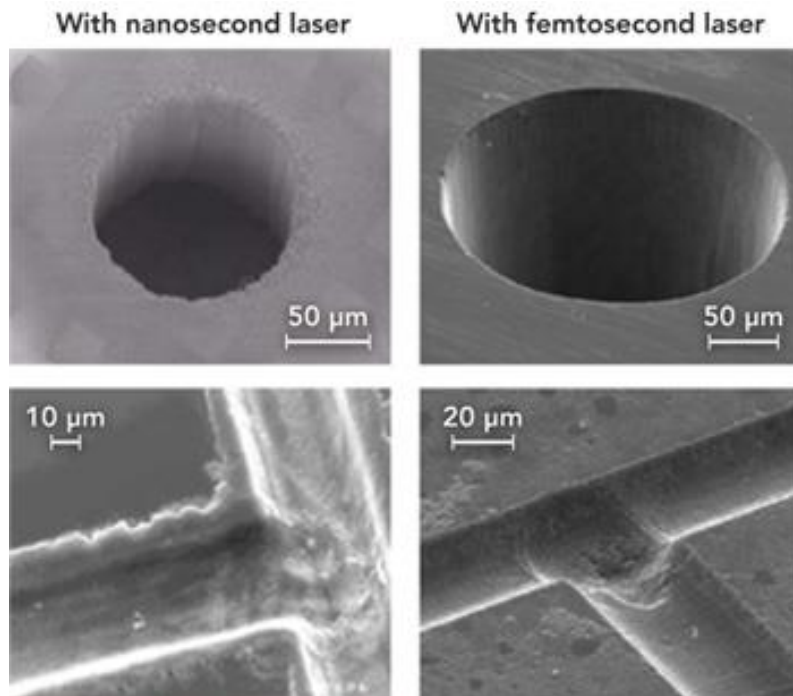


Fig. 4: (Top-left) Nanosecond 255 nm UV laser ablation crater in glass. (Bottom-left) Same laser projected through mask to create a channel. (Top-right) Femtosecond 780 nm laser ablation crater in glass. (Bottom-right) Same laser projected through a mask to create a channel²¹.

In the nanosecond regime, a laser pulse ablating a material causes evaporation and melting on the surface of the material. This is because the ablation is dominated by free electron heating due to inverse bremsstrahlung. The relatively long pulse also causes the ablation crater to spread out in comparison to craters created by femtosecond laser pulses²². As shown in Figure 4, the femtosecond pulse duration is too fast for thermal processes to take

place in the material, thus eliminating energy-losing vaporization and the melting ring present around nanosecond ablation craters²³.

Lasers also offer the flexibility to switch between their fundamental wavelength and their harmonics to tailor photon energy to the ionization energy of the compound one is interested in, which in turn reduces fragmentation. Another advantage is that LA-ICP-MS lasers can ablate down to a pico-liter volume out of a glass or other solid sample²⁴. Solids, and glasses in particular, are studied by laser-based mass spectrometers for a wide variety of reasons. One reason to analyze glasses using laser ablation is to identify elemental differences to determine where they originate from¹³. Some are analyzed to study molecular structures, such as Laser-induced Ionization Time of Flight Mass Spectrometry (LITOF-MS) investigating metal oxide structures²⁵, or LA-ICP-MS analyzing sulphide glasses to improve future thin film deposition²⁶. Other times glasses are analyzed to determine how different levels of dopants can affect the glass on a molecular level. For example, a study of diffused lithium isotopes of different molar masses in glass used a LA-ICP-MS to determine concentration and how mobile the ions were on their own¹⁵. In general, this laser ablation mass spectrometry is very useful in analyzing inorganic molecules in dense, solid materials, such as glasses.

1.3 Secondary Ion Mass Spectrometry: TOF SIMS and Dynamic SIMS

Another very prominent mass spectrometry technique in the analysis of solids and thin films is Secondary Ion Mass Spectrometry (SIMS). SIMS is split into two modes, the static mode and dynamic mode. Whether a SIMS instrument is operating in static or dynamic mode is determined by the primary ion dose, with 10^{12} ions/cm² being the “static limit^{26,27}.” Operating

the primary ion source higher than the static limit puts the instrument in dynamic mode. Since SIMS can be operated in these different ion dose regimes, different SIMS methodologies are used in conjunction with each mode. SIMS TOF uses a primary ion source in static mode along with a time-of-flight mass analyzer. This technique focuses on analyzing atoms and molecules from the top few monolayers of the surface of a sample²⁸. Dynamic SIMS operates the ion source past the static limit and commonly uses either a magnetic sector or quadrupole instrument for detection. SIMS TOF uses a lower energy ion beam than dynamic SIMS which allows molecules to remain intact, but also makes the instrument very sensitive to the cleanliness of the surface²⁹. Since the technique can detect molecular ions and uses a TOF, it is used for a variety of imaging applications. SIMS TOF has been a staple in composition mapping for some time, and just as recently as 2014 it was able to achieve better than 100 nm lateral resolution³⁰. A schematic of a SIMS TOF instrument is shown in Figure 5²⁹.

In contrast, dynamic SIMS uses an ion source with a much greater ion current, which allows the instrument to conduct a bulk, quantitative analysis of the sample without being affected so much by the surface conditions³¹. The higher energy ion source fragments any molecules during the sputtering process, which is where energetic primary ions bombard the surface of a sample. Dynamic SIMS is mainly used for isotopic and elemental analysis. SIMS has been used extensively to study the composition of glasses³²⁻³⁵. The detection limits of SIMS TOF are between 10-50 ppm for different isotopes. Dynamic SIMS can detect all the way down to the ppb level^{34,36}. This makes these ion-based analytical methods attractive for detecting low-concentration dopants in glasses. SIMS, which has been around for over 65 years, is mainly

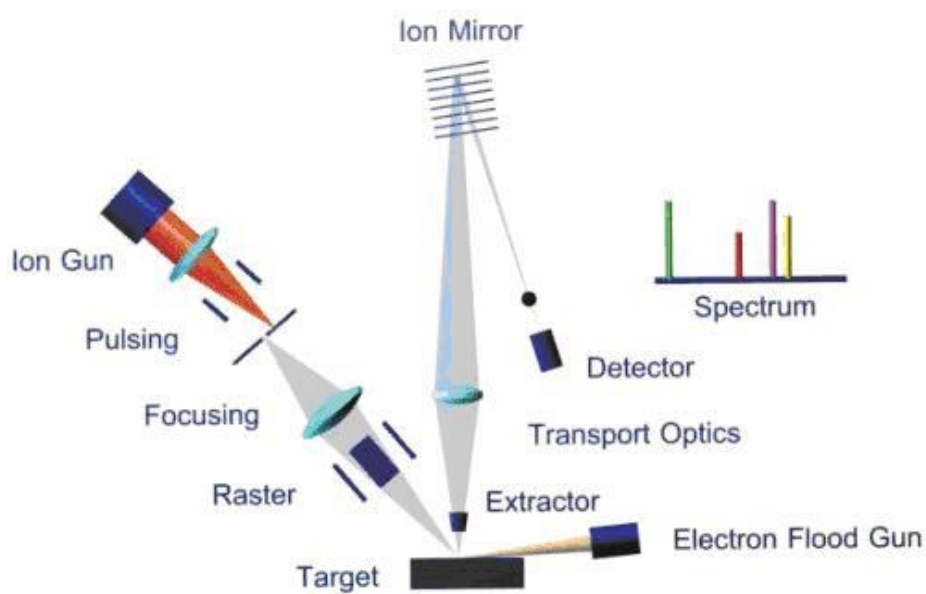


Fig. 5: Schematic of CAMECA IonTOF SIMS TOF instrument²⁹. The ion gun rotates back and forth across the initial slit to create a pulsed ion beam.

used in conjunction with other techniques such as ICP-MS and Thermal Ionization Mass Spectrometry (TIMS) to analyze trace components of glasses³⁷.

1.4 EUV Mass Spectrometry

Extreme Ultraviolet Time-of-Flight Mass Spectrometry (EUV TOF) is a relatively new technique, compared to the more established LA-ICP-MS and SIMS, and it was first demonstrated at CSU⁴. EUV TOF falls under the umbrella of laser-based mass spectrometry, but one major difference is its ability to ablate and ionize material using only the laser pulse. This is possible due to high-energy EUV photons, which for a 46.9 nm laser corresponds to 26.4 eV photons. At this energy, the photons are able to ionize any element on the periodic table, even gases such as helium and neon which have ionization energies above 20 eV³⁸. Prior experiments

in laser ablation mass spectrometry in solid samples using a 46.9 nm EUV discharge laser have been done at Colorado State University by Ilya Kuznetsov and collaborators^{4,39,40}.

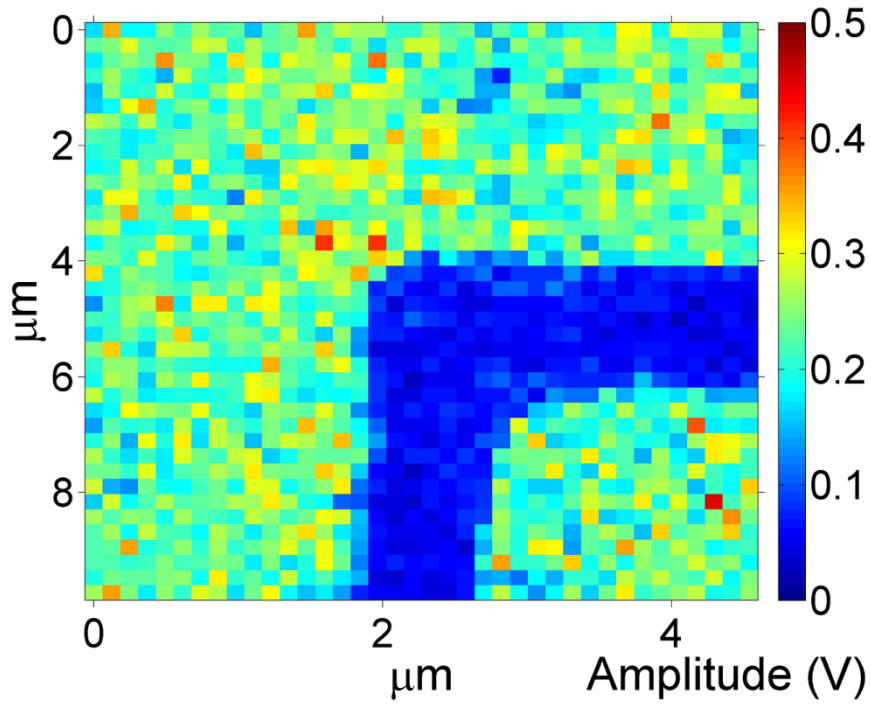


Fig. 6: A composition map⁴ of a 10-by-10 micron area where an L-shape was etched out. The colors represent the mass peak intensity of photoresist detected in each pixel by the EUV TOF.

Experiments in gas phase samples using the 46.9 nm EUV source for ionization were carried out by E. Bernstein and collaborators^{41,42}. The former's work focused on characterizing EUV TOF and determining its spatial resolution and imaging ability on organic samples. An example of this is shown in Figure 6⁴. The latter focused on the high photon energy of the EUV source to study the single photoionization of a variety of inorganic and organic clusters^{41,42}. Despite having very high-energy, 26.4 eV photons that contribute to fragmentation, experiments have shown the technique to be able to detect intact molecules⁴.

1.5 NIST Calibration Glasses

Just about every analytical mass spectrometric technique has used NIST glasses for calibration and characterization including TIMS, SIMS, and LA-ICP-MS^{14,33,35,43,44}. NIST glasses, especially SRM 610 and 612, are regarded throughout the field as highly-standardized reference samples that can be used to calibrate a mass spectrometry system, determine the sensitivity threshold of the technique, and allow for the comparison of detection sensitivities across mass spectrometric techniques for over 60 different elements⁴⁵. NIST SRM 610 and 612 glasses have nominal isotopic concentrations of 500 ppm and 50 ppm, respectively^{46,47}. Lesser-used NIST glasses of SRM 614 and 616 have nominal concentrations of 1 ppm and 0.02 ppm respectively, although the concentration for a specific isotope can vary from this nominal value substantially^{48,49}. Samples of NIST 610, 612, and 614 are shown in Figure 7⁵⁰.

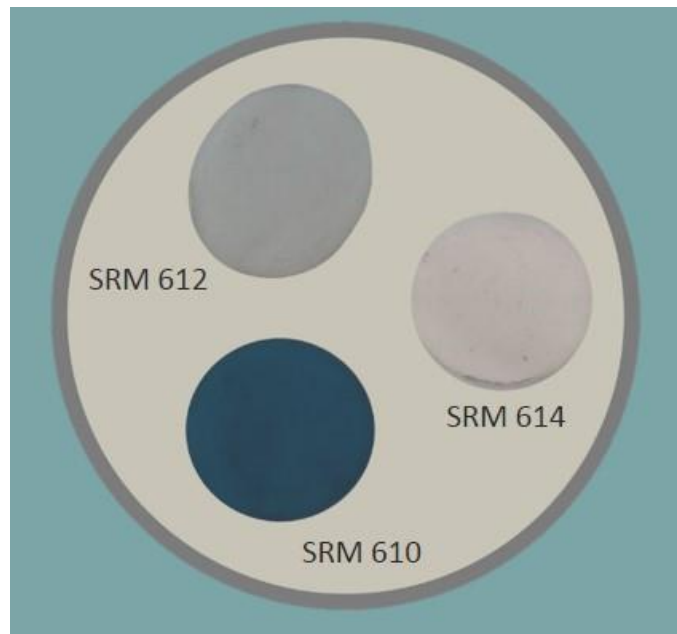


Fig. 7: NIST glasses SRM 610, 612, and 614⁵⁰. The color of the glass is progressively darker as the concentration of dopants is higher.

The content of NIST 610, 612, 614, and 616 is detailed in the manuscript “Determination of Reference Values for NIST SRM 610–617 Glasses Following ISO Guidelines” by K.P. Jochum, et al.⁴⁵. It is important to note that the difference between NIST SRM 610 and 611 is only glass thickness. The same applies for the other three glasses and their corresponding odd-numbered SRMs. The distribution of the doped isotopes in these glasses has also been studied and found to be highly uniform⁴⁵. This is very important for laser-based techniques which would ablate an area of the glass ranging from 100’s of microns to 100’s of nanometers in size and still expect to detect all of the doped isotopes.

1.6 Nuclear Forensics

The field of nuclear forensics is relatively new, the term being coined in the early 1990’s, and one of the detection methods used is mass spectrometry⁵¹. Figure 8 shows the timeline of nuclear material seizures that have driven advancements in nuclear forensics. Several other methods aside from mass spectrometry are used, including alpha-particle and gamma ray spectroscopy, scanning electron microscopy, and x-ray fluorescence. Mass spectrometry provides the most sensitive analytical approach to identify specific isotopes and to determine the age of the nuclear material⁵².

Reported weapons-usable nuclear material seizures

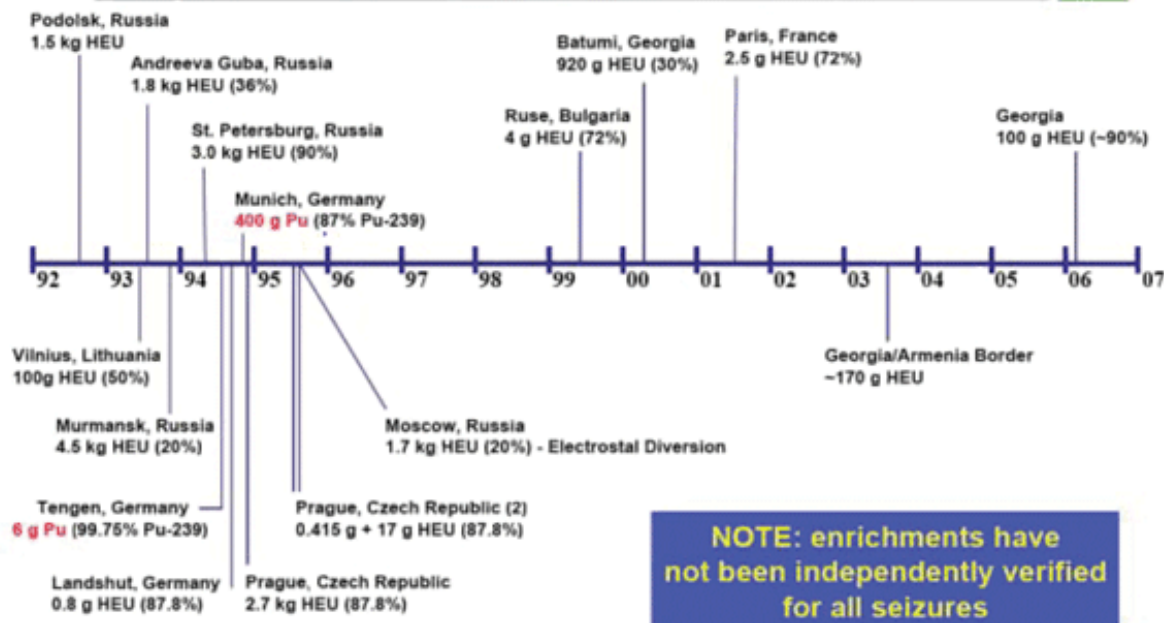


Fig. 8: Timeline showing the seizures of nuclear material from 1992 to 2007⁵³. The initial seizures of the early 90's spurred the creation of the field of nuclear forensics and is the driving force behind it.

Some of the most common mass spectrometric techniques currently in use for nuclear forensics are TIMS, MC-ICP-MS, and SIMS, with each technique having certain advantages and drawbacks^{54–56}. TIMS is able to detect ultra-trace (ppb or lower) amounts of nuclear material and identify isotopic ratios with excellent precision, but this technique requires extensive sample preparation and can have difficulty in detecting isotopes of similar mass^{57,58}. MC-ICP-MS has many of the same qualities as TIMS and is in some ways replacing TIMS as a gold-standard of isotopic analysis⁵⁹. The analysis is able to be done much more quickly than with TIMS and is able to identify isotopes with higher ionization potentials, but its operation can generate more artefacts in the data than TIMS and requires more quality control and calibration to precisely

analyze a sample⁶⁰. Finally, the remaining wide-spread mass spectrometric technique for nuclear forensics is dynamic SIMS. This method is useful because it can sputter a sample and scan over a large area on the scale of minutes to hours⁵⁴. The downsides are that it cannot perform a quantitative analysis as well as the other methods and its results are matrix-dependent, as well as needing the sample to be very flat and conductive⁶¹.

Looking towards the future an ideal analytical mass spectrometry method would be able to analyze suspected nuclear material as is and perform the analysis in a short time without the need of overly expensive equipment or extremely skilled operators. It should also be able to identify ultra-trace amounts of uranium and plutonium isotopes, as well as their daughter isotopes and other trace elements in order to determine the age of the material and its origin. While no system currently exists that can perform all of these functions, current methods are able to complement each other to provide many of these aspects all together⁵².

1.7 Overview of the Thesis

One of the purposes of the research described in this thesis is to demonstrate the capability of the EUV TOF system for the analysis of inorganic materials, to further characterize the system and compare it to other industry standard methods, and to determine its imaging potential on metals and oxides. Towards this goal, a thorough diagnostic of sources of noise that raise the baseline signal or cause voltage spikes that necessitate the pulse gating of the detector have been undertaken.

To pursue the characterization of the system, well-structured, well-known samples were needed for analysis. For trace isotope analysis, NIST glasses were used due to the large amount

of documentation detailing the concentrations of isotopes doped in the glass, and these documents have also allowed a one-to-one comparison on the isotopes that were measured. For the resolution assessment, a sample made out of electroplated nickel and gold interleaved comb structures was used. It is shown that the instrument has a lateral resolution of 80 nm when imaging these structures. This measurement's analogue on an organic sample determined the spatial resolution to be 75 nm⁴. Imaging was demonstrated on micron-sized enriched and natural uranium particles to map out a high-resolution isotope composition image.

The EUV TOF system is affected by excess background noise emanating from the multi-channel plate (MCP) detector. This noise reduces the signal-to-noise ratio of all detected mass peaks, and it increases the amount of data collection needed to view trace isotopes in an averaged mass spectrum. When analyzing the NIST glasses, it was impossible to discern several trace elements without averaging multiple spectra together due to the noise level. A background noise analysis was conducted to diagnose the cause of the background noise and reduce the noise level by an order of magnitude.

This thesis is broken into 5 chapters. Chapter 2 describes the EUV TOF system and details all of its components. Chapter 3 presents the procedure and results of the background noise analysis, and describes how the noise issue was mitigated. Chapter 4 describes results of the characterization of EUV TOF on actinides and samples doped with trace isotopes carried out in collaboration with Pacific Northwest National Laboratory (PNNL). Chapter 5 summarizes the results of this study and describes future work.

Chapter 2: Description of the EUV TOF Mass Spectrometry System

2.1 Overview of the system

The EUV TOF system is a mass spectrometer that uses a 46.9 nm EUV capillary discharge laser as an ablation/ionization source and a Time-of-Flight mass analyzer with a multi-channel plate detector. A top-down representation of the system is shown in Figure 9.

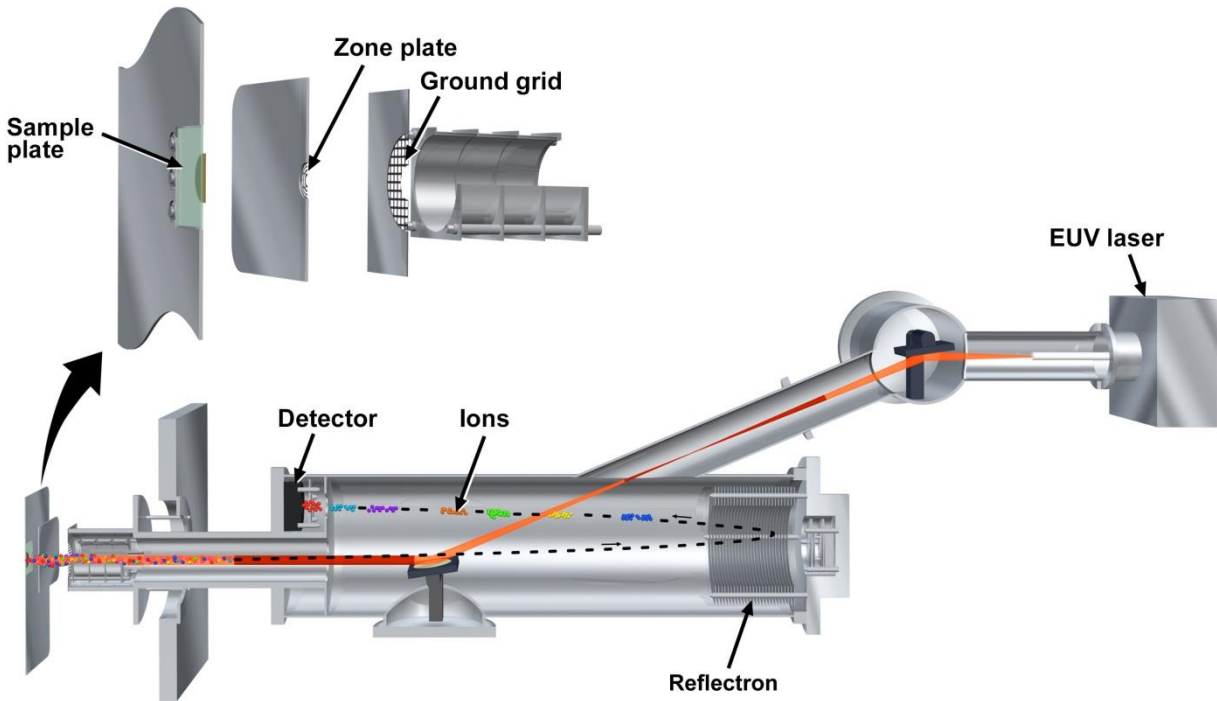


Fig. 9: Diagram of the EUV TOF system showing the EUV pulse path as an alternating orange and red line, and the ion path as the dotted black line with ion groups represented with various colors.

The compact EUV laser, first demonstrated by Rocca and collaborators^{62,63}, operates by ionizing argon atoms to a neon-like state and producing EUV stimulated emission at 46.9 nm via

collisional electron impact excitation. The duration of the laser pulse is \sim 1.5 ns FWHM, it has an average pulse energy of $13 \mu\text{J} \pm 1.3 \mu\text{J}$, and has a laser linewidth around $1*10^{-4} \Delta\lambda/\lambda^{62,64}$.

A General Atomics power supply provides a 60kV, 80 ms discharge that ionizes argon gas inside a 3.2-mm wide, 18.5 cm long alumina capillary into a low ionized state. This begins the formation of a plasma column that allows for better magnetic compression along the length of the capillary. 100 μs before the pre-pulse finishes, the large spark gap closes its connection and discharges the primary pulse that was stored in the 20 capacitors surrounding the spark gap. Simultaneously to the large spark gap closing, an additional pre-pulse is applied directly to the anode which ionizes the argon gas even further. The main current discharge around 22kA creates a magnetic field that encircles the argon plasma column and shrinks and pinches the column. This raises the electron temperature inside the column and increases the collision rate of the neon-like argon ions, thus making collisional electron impact excitation favorable and leading to 46.9 nm amplification. 5-8 ns later, the electron density reaches a maximum inside the capillary and lasing ceases due to the electron density causing increased refraction and the collision rate lowering due to collisional thermalization.

The EUV laser pulse is focused onto the sample with a zone plate to ablate the material which forms a plasma between the sample and zone plate. Inside this plasma, some of the atoms undergo single-photon ionization and become positively ionized, some of the atoms pick up an electron and become negatively ionized, and the rest remain neutral and eventually drift off. The extraction and repeller plates bring positive ions up to an energy of 6 keV where they drift towards a reflectron that turns the ions around toward the multi-channel plate (MCP)

detector. During their flight, the ions are separated in time depending on their mass as described in section 1.1.

2.2 Details of the System

The EUV laser and TOF chamber are separated by a mirror transfer chamber that allows the laser pulse to be redirected. The laser is housed in an enclosure that measures approximately 0.4m by 0.4m. Inside the enclosure is a large spark gap surrounded by 20, 3500 pF capacitors arranged in a 10-by-2 parallel-series configuration, as shown in figure 10⁶⁵. The enclosure is constantly circulating eco-friendly transformer oil using a chiller to dissipate the intense Ohmic heat generated by the 22 kA pulse and to insulate the parts to avoid electrical arcing. The EUV laser is powered by two power supplies, one manufactured by Maxwell and the other by General Atomics. The General Atomics supply is responsible for supplying the preionization pulse to the capillary, charging the six, 40 nF, 35 kV capacitors inside the pulser, and the twenty capacitors housed in the EUV laser enclosure. The Maxwell supply is responsible for closing the spark gap inside the pulser which activates the main laser discharge. This is demonstrated in more detail in figure 11⁶⁶.

The power supplies are triggered by a 5 V, TTL square pulse from a Stanford DG535 digital delay generator. Argon gas is flowed into the chamber that houses the capillary, and that is differentially pumped using a 2 mm pinhole aperture located at the exit of the capillary to keep the argon pressure around 300 mTorr.

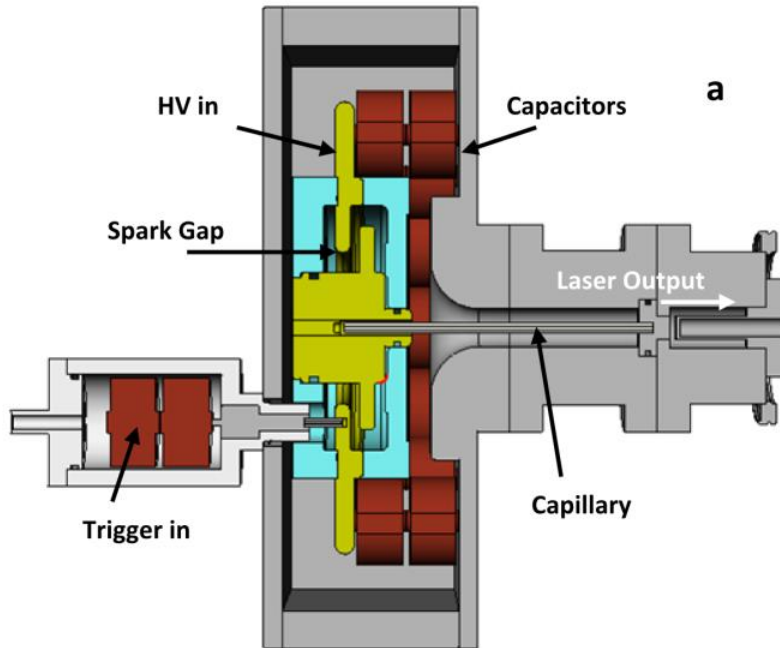


Fig 10: Side view of the 46.9 nm laser⁶⁵.

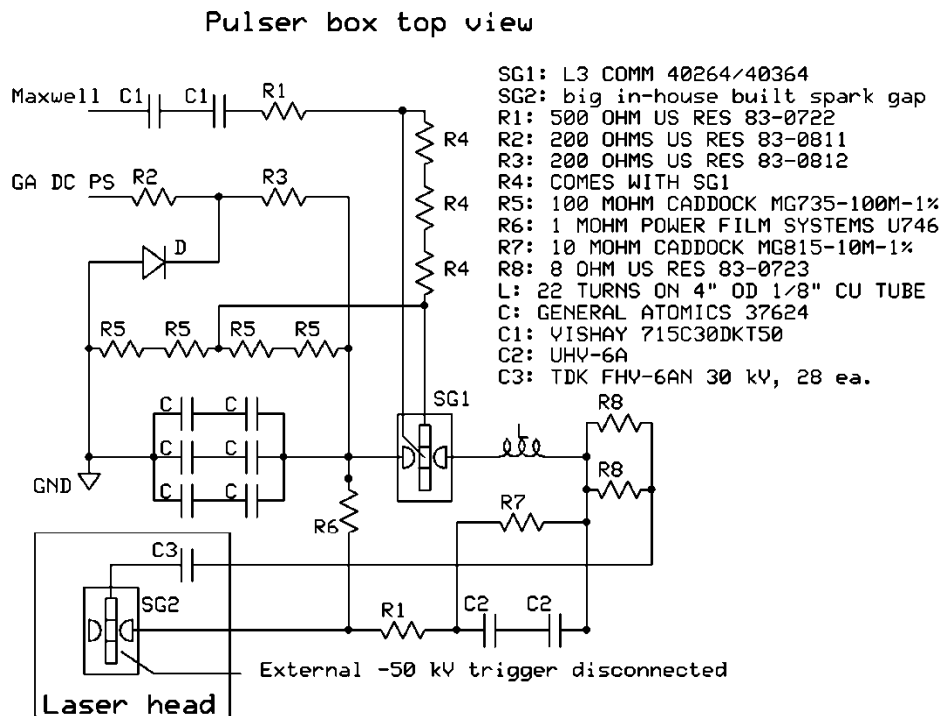


Fig. 11: Electrical schematic of pulser box⁶⁶. The pre-pulse and preionization pulse enter the spark gap through the R6 and R1 resistors. The main pulse is stored in C3 until triggered.

The system is set up to be differentially pumped such that the steady state pressure is 300 mTorr at the capillary and $\sim 10^{-7}$ Torr at the other end inside the sample chamber. Two silicon o-rings encapsulate the capillary and two o-rings are used with the cathode to keep oil from leaking into the vacuum system. Placed around the cathode is a Rogowski coil in which a current is induced by the high-voltage laser pulse. The coil is used to trigger various electronics throughout the system. Immediately after the capillary chamber is the gas cell. This cell has apertures on both sides to for pressure control and to isolate it from the rest of the system. The cell can be flowed with argon using a slip valve to attenuate the energy of the laser. A scroll pump is attached to the bottom of the gas cell. The chamber after the gas cell has a turbo pump and scroll pump attached to its top, a glass Bayard-Alpert ionization vacuum gauge attached on its side, and a gas photoionization detector. The nominal pressure inside this chamber is $\sim 5 \times 10^{-6}$ Torr. Between this chamber and the mirror transfer chamber, there is another aperture, an automatic valve in case of leaks, and a retractable aluminum photodetector. The automatic valve is pressurized around 60 PSI and shuts if the vacuum pressure rises suddenly. Both the aluminum photodetector and gas photoionization detector are powered with Stanford PS350 high voltage power supplies with 1500 V and using a circuit box that delivers the power and outputs the detector signal. These chambers and components comprise the EUV laser section of the system.

The mirror transfer chamber houses a gold-coated toroidal mirror and a gold-coated flat mirror which reflect the EUV beam with $\sim 70\%$ efficiency. They are mounted on a bar controlled by a Thorlabs motor, and the toroidal mirror can be tilted in x and y using separate Thorlabs motors. The purpose of the transfer chamber is to direct the laser pulse either into the TOF

chamber or into a chamber used for microscopy. This section is pumped by a scroll and turbo pump combination. There is an aperture and a MDC gate valve that separates this chamber from the TOF chamber which is kept around 10^{-7} Torr. The TOF section of the system consists of the TOF chamber that houses the mass analyzer and detector and the sample chamber which houses the sample, zone plate, viewing microscope, ion optics, and various motors. A diagram of the TOF chamber is shown in Figure 12.

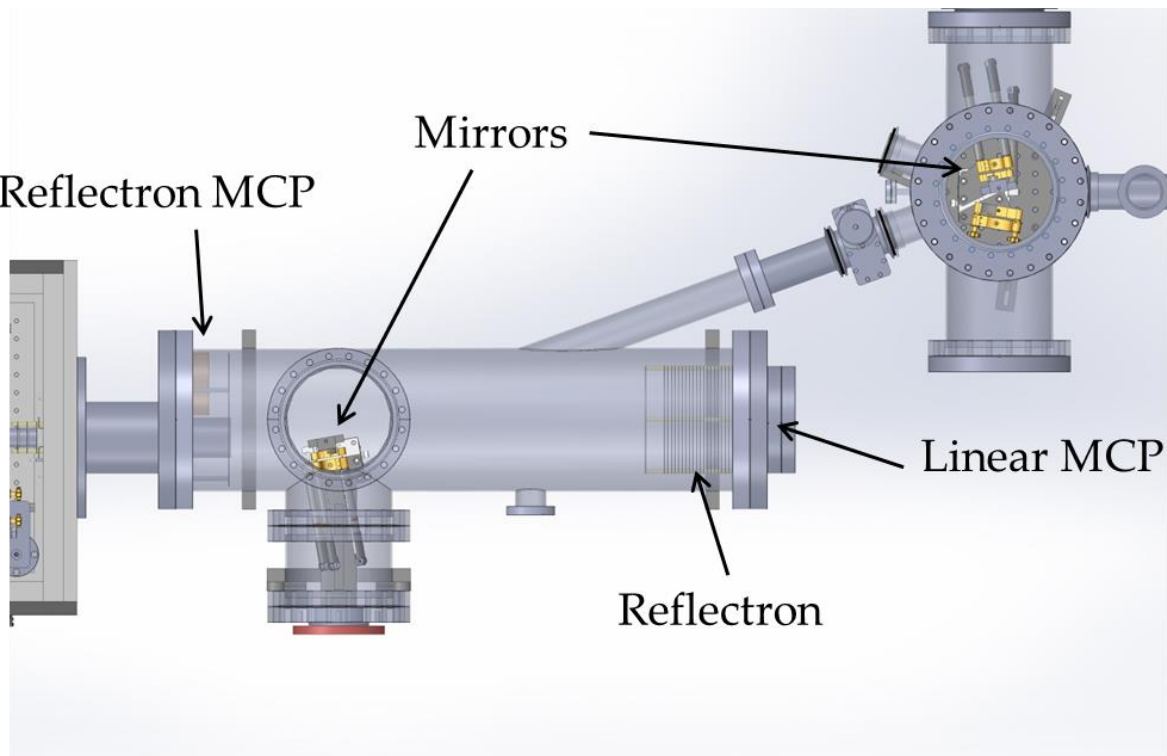


Fig. 12: Top-down schematic of TOF chamber on the left and mirror transfer chamber on the right. The objects in yellow are mirror mounts.

The stainless-steel TOF chamber houses two MCPs, the reflectron-mode MCP being on the top-left of the chamber in figure 12, and the linear-mode MCP being on the right in the figure. The linear-mode MCP has an 18 mm active area diameter, while the reflectron-mode MCP has a 40 mm active area diameter. It needs a larger area because the ions can spread out

further laterally over a longer flight path. The dual-stage reflectron is made of the retarding grid, which the ions initially encounter, and several voltage plates commonly set at 7 kV. The retarding grid is set between 4300-4700 V, but needs to be optimized before each experiment depending on what the sample is and what isotopes the experimenter is looking for. The reflectron helps to diminish the effect of temporal ion spreading caused by a range of initial kinetic energies by compressing ions together that have the same m/z ratio. The smaller flange in figure 12 seemingly not connected to anything is connected to a KJLC 979 wide-range transducer which can measure pressure from atmospheric to 10^{-10} Torr.

There is one gold toroidal EUV mirror attached to a stage and three Thorlabs motors that can tilt the mirror in the x-y plane, as well as translate it in the z-axis. The toroidal mirror in the transfer chamber reflects the EUV beam 15 degrees, and the second toroidal mirror in the TOF chamber returns the beam to roughly 0 degrees to fully illuminate the zone plate. Above the TOF chamber, not shown in the figure, is a turbo pump and large valve that can be closed to isolate the turbo pump from the rest of the chamber. Since the cable connecting the turbo pump to its controller is longer than it should be, this can cause inductive feedback and sometimes lead to pump failure while starting up. This valve allows the operator to leave the turbo pump on if the sample chamber needs to be opened quickly so that they won't get delayed by the controller failing on startup.

The sample chamber houses a few ion optics, the sample holder, the zone plate, the microscope, and several motors, stages, and connectors. The ion optics include the deflection plates, an Einsel lens, and the extraction and repeller voltage plates. The deflection plates are set between 0-500 V and have to be optimized similarly to the retarding voltage. When

optimizing, the retarding voltage needs to be set such that the mass peaks are sharp and symmetrical. The deflection plate voltage should be set to maximize the intensity of the mass peaks and minimize their full width at half maximum (FWHM), making sure it is at least below 20 ns. The Eisel lens is used to focus the ions as they begin their journey into the TOF chamber. This lens is commonly grounded while the system is configured to detect positive ions because no difference is observed in this mode whether the lens is set at 0 V or 2 kV. This lens is set to -4 kV, however, while the system is configured to detect negative ions. The reason for this is most likely because the voltage potential between the extractor and repeller plates is only 700 V in negative mode compared to 5 kV in positive mode. This lower energy potential allows the initial kinetic energy of the ions to contribute to a greater degree leading to ions spreading out more before reaching the lens. The repeller voltage plate is made of a stainless steel sample holder that holds a conductive 1 inch by 1 inch glass sample. The sample holder is shown in figure 13.



Fig. 13: The sample holder unscrewed from the PI piezo stages. The glass slide is attached via six screws, three on each side.

The repeller plate that holds the sample is charged to 6 kV. It is very important that the sample be conductive to provide a uniform electric field to repel formed ions. A non-conductive sample is usually evaporated with 10's of nanometers of a metal coating, such as aluminum or gold, making sure that the coated metal does not produce interferences with isotopes of interest on the sample. Positive ions are repelled by the 6 kV plate, travel through the extraction plate charged at 1 kV, then reach the ground grid with an overall energy of 6 keV. The extraction plate is made up of a conductive zone plate held by a stainless steel holder placed 2.1 mm from the sample holder. A close-up of the zone plate is shown in figure 14.

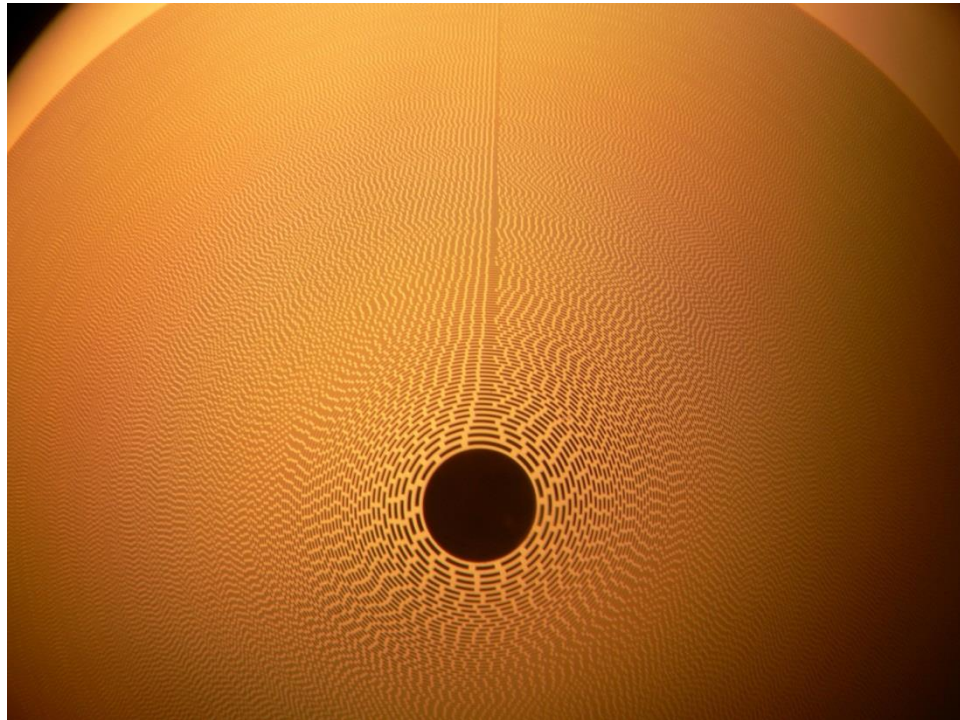


Fig 14: Close-up of the zone plate. The central 50 μm diameter opening allows ions to pass through and into the mass analyzer.

The zone plate is used to focus the EUV laser beam onto the sample. The zone plate has a central opening of 50 microns and an outer zone width of 200 nm. Its first order focal length is 2.1 mm. The extraction plate is charged to 1 kV, which was found to provide the best signal intensity in a previous experiment by Ilya Kuznetsov. Beyond the extraction plate is a grounding grid set at 0 V. The ions are accelerated to an energy of 6 keV overall.

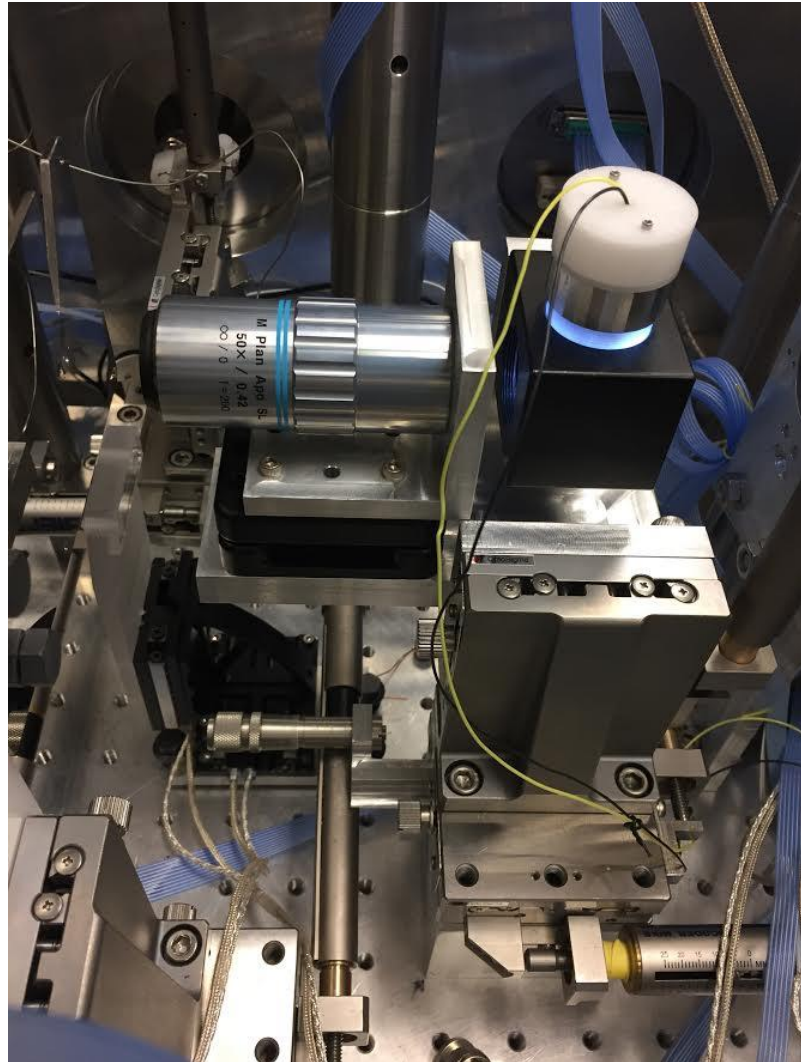


Fig. 15: The objective microscope assembly. Shown is the 50x objective lens, LED lighting, and to the right of the image outside of the chamber would be the CCD camera.

A microscope objective placed inside the sample chamber is used to align the sample at the zone plate focus and track ablation craters that are made on the sample. The microscope is equipped with a black-and-white Mightex CCD camera. The image the camera receives is lit by a cylindrical set of LED lighting and is focused by a 50x objective lens onto the sample. The objective and LED lighting assembly are shown in figure 15. This is sufficient to view ablation craters, that look like black dots, that are only a few hundred nanometers in diameter. The zone plate and objective lens each have two Thorlabs motors which control their x-y motion which is in the plane of the sample and perpendicular to the incident beam. An ORIEL Encoder Mike Controller Model 18011 controls their z-axis motion with micron precision. The sample x-y motion is controlled with two PI piezo stages that are accurate down to a few nanometers. These stages allow an operator to conduct nanoscale-resolution composition mapping of a sample.

The last section of the EUV TOF system is the external electronics. There are 4 separate Stanford PS350 high voltage power supplies that power the aluminum photodetector and gas photoionization detector, the deflection plates, the Einzel lens, and the MCP. When a current is induced in the Rogowski coil, this current provides a trigger pulse for the MCP and the computer digitizer card, telling it to begin acquiring spectra. In order to activate the MCP, the Rogowski coil signal triggers a Stanford DG535. The delay generator can be set with a time delay down to 1 microsecond to prevent lower masses from being acquired if they are too intense. The DG535 sends out a delayed signal to a trigger box which delivers -2200 V into a voltage divider. This voltage divider provides -2200 V to the plate closest to the active area,

-1200 V to the middle plate, and -200 V to the farthest plate from the active area. A Tektronix TDS 7404 oscilloscope is used to collect and display signals from the two photodetectors and the Rogowski coil. There are also 4 turbo pump converters that provide power and frequency control to the turbo pumps and two, four-channel high-voltage power supplies made in-house that provide power to the voltage plates used for ion acceleration and extraction. There are two of them because one is able to generate positive voltages when the system is extracting positive ions, and the other can generate negative voltages when the system is extracting negative ions. The external electronics used in mass spectra collection are connected starting at the output of the MCP. The MCP output signal first travels through attenuators and an Ortec VT120C preamplifier. The preamplifier is used to eliminate signals longer than \sim 1 μ s and amplifies the signal 20x. The three attenuators, two 10x attenuators and one 4.44x attenuator, reduce the amplitude of the signal so that the maximum intensity does not exceed 250 mV at the input of the preamplifier, and therefore 5 V at the digitizer card. The attenuators and preamplifier can be mixed and matched to have an overall attenuation as high as 444x or have an overall gain of 20x, with many delineations in between. These input voltages are their specified limits.

After the preamplifier, the signal travels into the digitizer card that is housed in a computer. This card is triggered to start acquisition by the signal from the Rogowski coil. The digitizer card is an EON CompuScope digitizer card with a maximum sampling rate of 1 GS/s. This means that when spectra is acquired, it is automatically digitized in 1 ns bins. The digitized signal from the MCP can then be viewed using Gagescope software, or collected and organized using a custom-made LabVIEW VI. This VI is used to map images by setting up a grid pattern

where the operator can specify how many craters should be made in x and y, how many laser pulses should be fired at each location, and what the spacing should be between locations.

Finally during analysis, the spectra are normalized by multiplying each data point by the overall attenuation divided by the amplification. This normalization counteracts the changes in amplitude caused by the attenuators and preamplifier. The spectra after normalization have the same amplitudes as the signal when it is produced from the MCP. Many different voltages have been stated in this section for both positive and negative ion collection modes. Table 1 summarizes the voltage settings and ranges for all adjustable voltage devices in the EUV TOF system.

Table 1: Nominal voltage ranges and settings for EUV TOF devices in positive and negative ion extraction modes.

Device	Nominal Voltage Range (Positive Mode)	Nominal Voltage Range (Negative Mode)
Multichannel Plate Detector	-2200 V	2200 V
Einsel Lens	0 to 2000 V	-4000 V
Repeller Plate	6000 V	-6000 V
Extraction Plate	1000 V	-5300 V
Reflectron	7000 V	-7000 V
Retarding Grid	4300 to 4700 V	-4700 V to -4300 V
Deflection Plates	0 to 500 V	-500 to 0 V
Aluminum Photodetector	1500 V	1500 V
Photoionization Detector	1500 V	1500 V
General Atomics Power Supply	60 kV	60 kV
Ortec Preamplifier	12 V	12 V

2.3 Samples Used in Analysis

The samples analyzed were NIST 611, 613, 615, and 617 glasses, a quartz slide from Lawrence Berkeley National Laboratory (LBNL) with nickel and gold interlaced comb structures, and a slide that contained micron-sized uranium oxide particles embedded in resist. All of the

samples had to be conductive in order to make an effective repeller for the ions, so the NIST glasses were coated with a thin (15-20 nm) layer of aluminum. The sample from Berkeley was metallic, and already coated with gold, and the uranium oxide sample was coated in ~30 nm of gold after it arrived from Pacific Northwest National Laboratory (PNNL). The NIST glasses were then taped onto a 1" by 1" microscope slide coated with indium tin oxide (ITO) with copper, vacuum-compatible tape. An image of NIST 611 and 613 glasses right before they were analyzed is shown in figure 16.

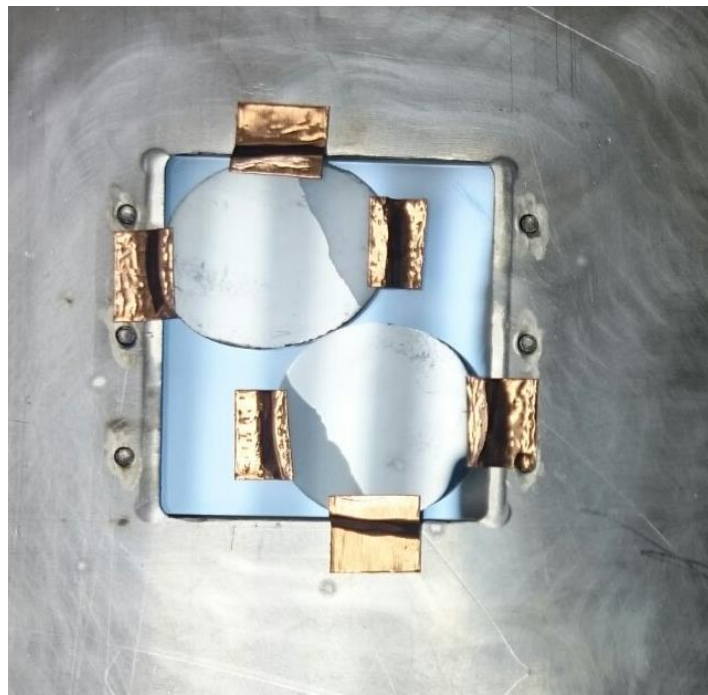


Fig. 16: NIST 611 and 613 glasses taped to an ITO-coated slide and the stainless steel sample holder with copper tape.

The NIST glasses were small enough to fit two of them onto a single slide, and this also allowed an accurate comparison between spectra obtained from NIST 611 and 613 since the spectra from 613 could be collected immediately after 611. NIST 615 and 617 were attached to

a separate slide, so the comparison between all four NIST glasses had to done by matching the laser pulse energy between the two experiments as closely as possible. Isotopes such as thorium or uranium yield peaks below the noise level in the spectra acquired with a single pulse, so 20-by-20-by-3 pulse grids were taken to increase the signal to noise ratio. The pulses in depth allowed us to view only the sample of interest as the aluminum coating and surface hydrocarbons are ablated off after the first laser pulse. This larger grid size was also chosen so that a 10-by-10 micron crater could be formed and analyzed on a white light interferometer.

Several preliminary scans were taken from the Berkeley sample in order to perfect the focus of the zone plate. These scans allowed the operator to maximize the argon attenuation of the laser pulse energy to achieve a small ablation crater size while also ensuring that the signal-to-noise of the nickel peaks would be adequate. The LBNL sample used for lateral resolution measurement is shown in figure 17.

The uranium oxide samples had only 9 pairs of uranium particles each, many of which were spaced more than 1 μm , which was too far apart to be able to acquire signal from both particles in the same scan. The scanned particles detailed in chapter 4 were labeled as U200-3. One of the particles was of natural uranium abundance, while the other had been enriched with U-235 such that the abundance of U-235 was 20%⁶⁷. Figure 18 shows the U500 sample. The U200 sample looks practically identical. The EUV laser was attenuated with argon gas to ablate smaller craters and achieve higher lateral resolution in the composition map image of the uranium oxide particles.

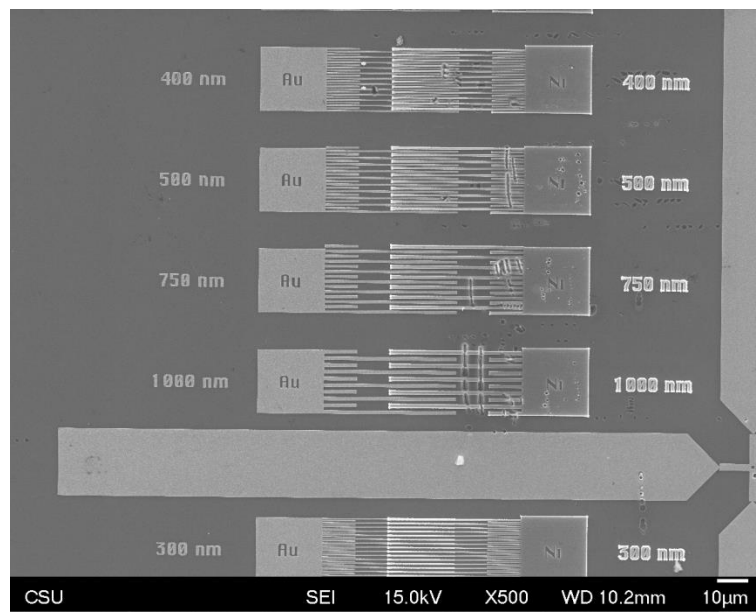


Fig. 17: A portion of the sample from LBNL. The gold comb structure is etched with an “Au” and the nickel structure “Ni.” The entire pattern is repeated 12 times on the entire substrate.

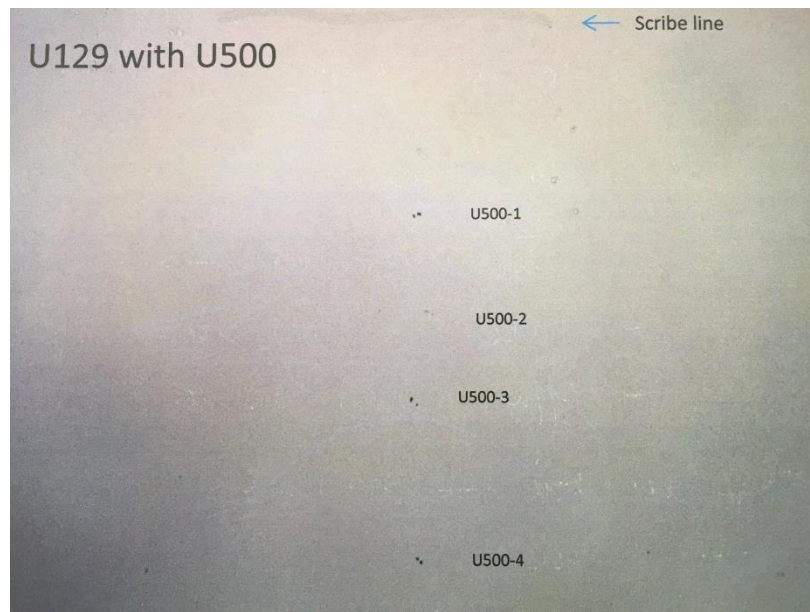


Fig. 18: The CRM U500 sample. The uranium oxide particles are highlighted in black in the image and labeled. The U200 sample looks very similar.

Chapter 3: Noise Source Identification and Mitigation

3.1 Noise Identification

There are two types of noise being generated on the MCP cable, as shown in figure 19.

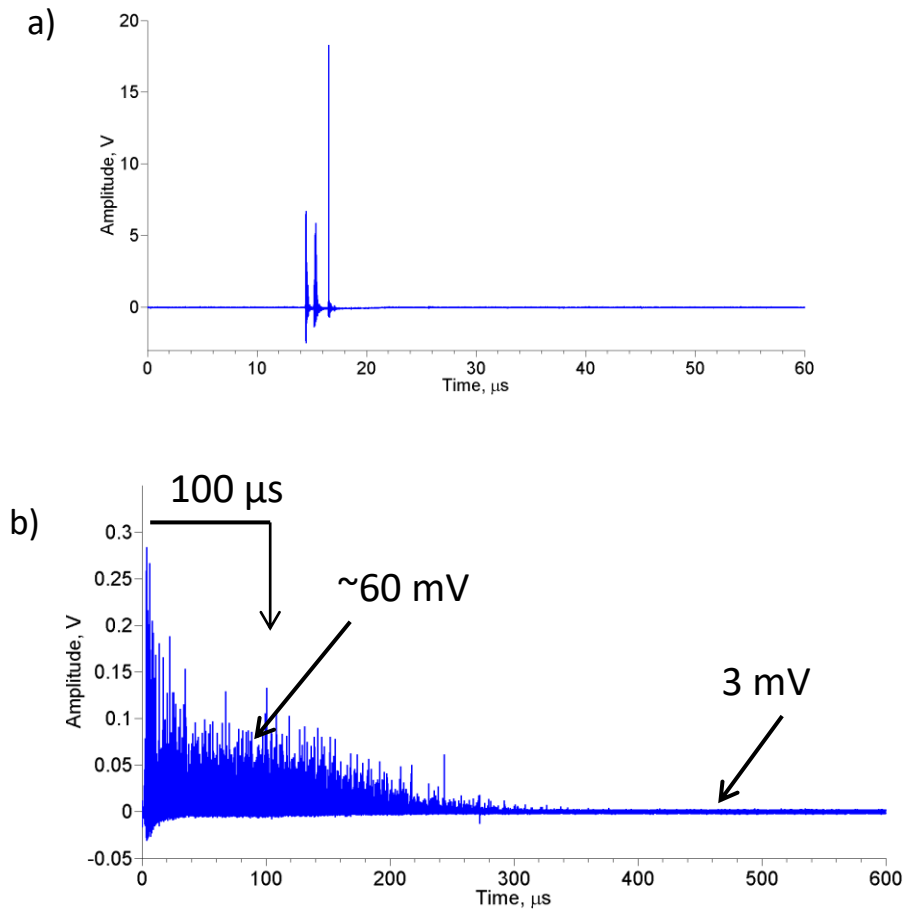


Fig. 19: (a) Pulses that appear prior to ion collection. Data acquisition was taken 16 μs before ions usually arrive with MCP powered with 1400 V instead of 2200 V. (b) A single-shot spectrum showing the noisy signal over a 600 μs data collection. The MCP is only active for the first 100 μs .

The first type of noise shown in figure 19a demonstrates that there are pulses on the MCP that are arriving prior to the time that ions would normally arrive. The first few pulses are isolated and are shown in figure 20.

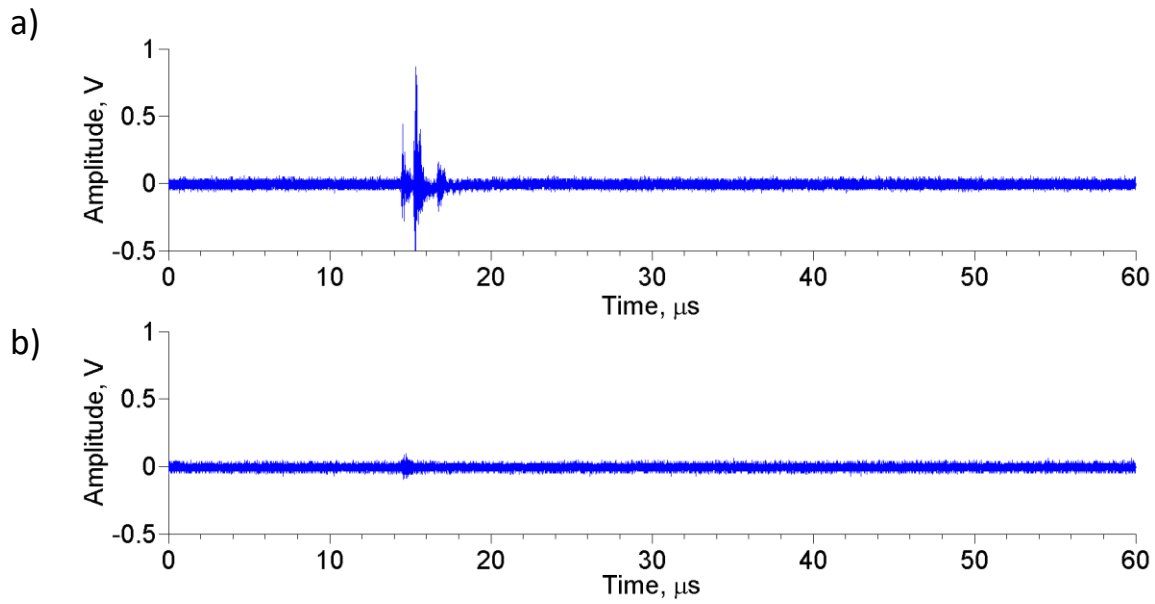


Fig. 20: (a) Pre-pulses that are due to reflections in cables connecting MCP to digitizer. (b) Signal after removing multiple cables from the MCP-digitizer link.

We identified the first few pulses to be caused by cable reflections that were successfully removed (figure 20b). Figure 19b shows the background noise lasting 300-400 μs that is ~60 mV in amplitude. In absence of the laser firing or after several hundred μs, the baseline electronic noise level is only ~3 mV in amplitude, so the initial assumptions were that lowering the background noise would be possible and that the cause was rooted in the system's operation. As described in chapter 2, the detection system consists of three MCP plates with voltages of -2200 V, -1200 V, and -200 V when operated normally. The MCP is located next to the entrance of the sample chamber, as shown in figure 12. Previously, a histogram analysis of uranium ion peaks from NIST glasses determined the MCP gain to be 18.5 mV/ion. In order to achieve the

minimum standard⁶⁸ signal-to-noise ratio (S/N) >3 of a mass peak in a single shot, the MCP would have to detect at least 10 ions of the atom or molecule of interest. This is not always possible when analyzing samples with trace amounts of isotopes. For example, the mass spectrum shown in figure 21a is from a single laser pulse ablating NIST 611 glass. After averaging 1,200 spectra, shown in figure 21b, peaks representing uranium, thorium, and other isotopes rise above the noise level, but these peaks cannot be discerned in the spectrum obtained with a single laser pulse.

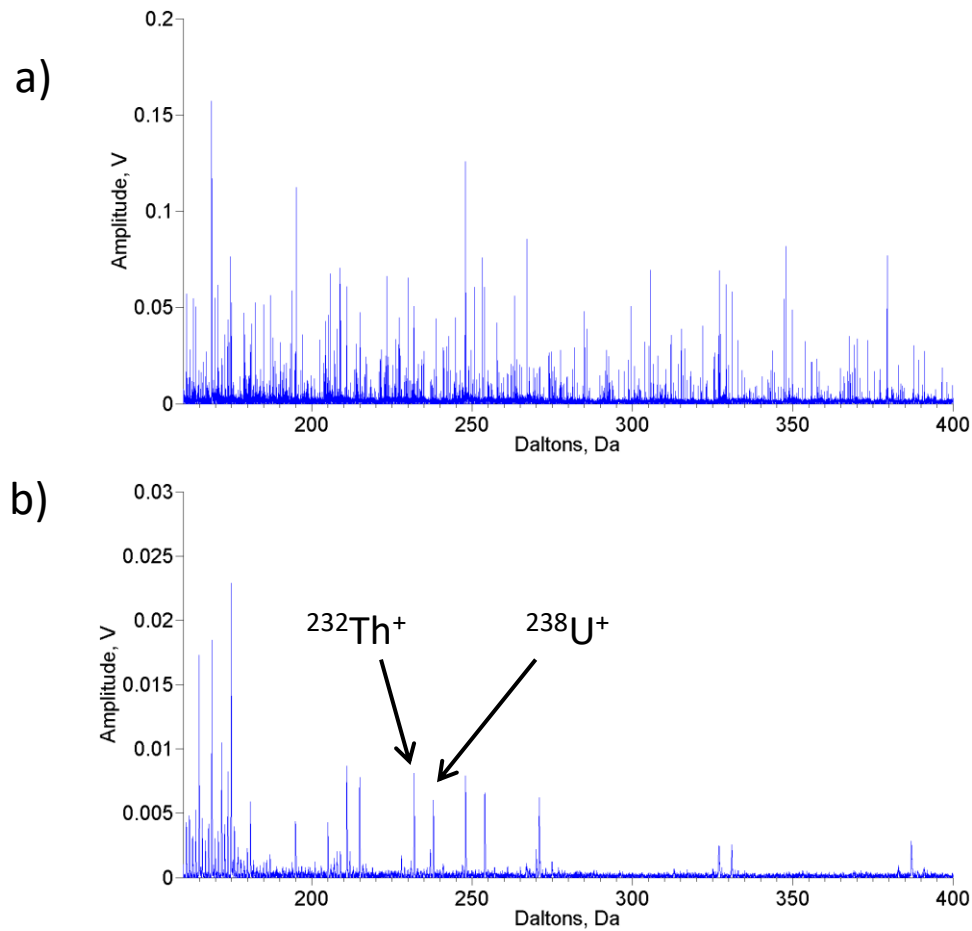


Fig. 21: (a) A single-shot mass spectrum from NIST SRM 611 glass taken with EUV TOF. None of the isotopes known to be present in the sample are clearly visible in the signal. (b) 1,200 mass spectra averaged from the same data set as 21a. Thorium and uranium positive ion peaks are labeled.

Multiple experiments were performed to systematically diagnose and identify the source of the background noise level. It was speculated that the elevated noise level could be photons from the laser discharge output interacting with the MCP or other electrical signals interfering with the MCP signal.

The first experiment performed to narrow down the cause of the background noise was to close the gate valve that separates the TOF chamber from the laser. The result is shown in figure 22.

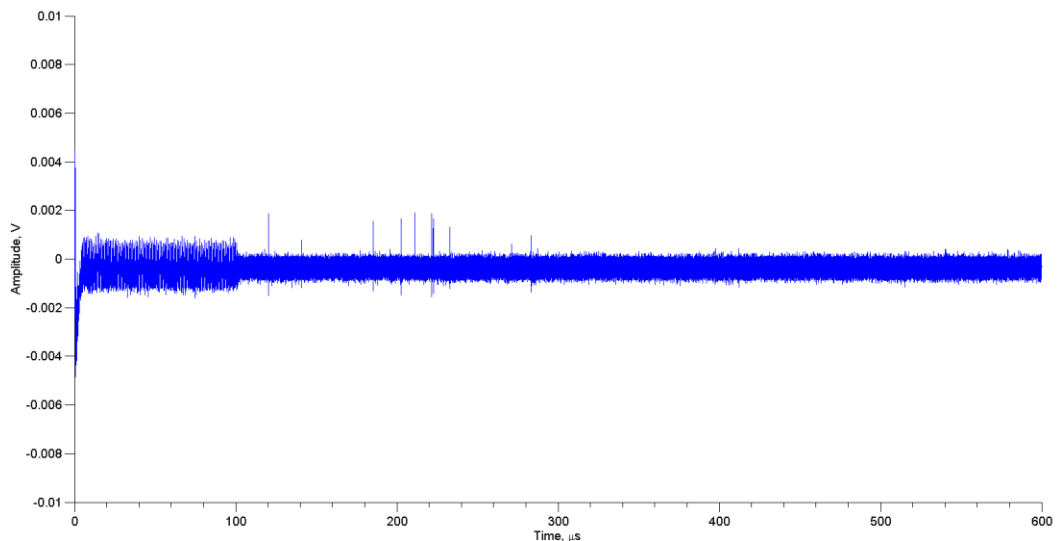


Fig. 22: The MCP signal collected with the gate valve closed averaged over 16 pulses. Additional noise is generated by the MCP when it is on, and it is clear that the MCP is deactivated after 100 μ s.

The background amplitude of figure 22 demonstrates that the noise shown in figure 21a is not being caused by electrical interferences. The noise only occurs when light from the capillary is able to enter the TOF chamber.

The next experiment focused on whether spontaneous emission from the laser occurring in the UV and VUV was interacting with the MCP. To test this, a 100-nm thick aluminum filter from Lebow Company was attached to a butterfly valve and placed in front of the laser output. The element aluminum was chosen for the filter since the transmission of 46.9 nm wavelength photons from the laser emission through a 100 nm-thick aluminum filter is 79%⁶⁹, while the transmission of the spontaneous emission above a wavelength of 80 nm is practically zero. The intensity of the laser after passing through the filter was measured on the aluminum photodetector so spectra could be collected in three different scenarios: at full laser intensity without being filtered (EUV+UV), with the same intensity laser pulse but filtered (EUV only), and with the unfiltered laser pulse attenuated to match the intensity of the filtered laser (EUV+UV). The collection time was set to 600 μ s in order to observe long-term behavior. The signals were all normalized as detailed in chapter 2, section 3. The preliminary results looking at the three different scenarios are shown in figures 23 and 24.

The data from figure 23 demonstrate that the background noise is shaped like a ramp, linearly decaying over the course of 300-400 μ s down to the minimum noise level of ~3 mV. The ramp noise does not decrease in any of the scenarios shown in figure 23, so UV radiation can be ruled out as a cause of the ramp noise. Moreover, the ramp noise lasts 3-4 times longer than the 100 μ s pulse applied to the MCP. From this we can conclude that the linear ramp noise is an electronic signal response and invariant to the presence of spontaneous emission.

The next experiment carried out consisted of acquiring data as in the three different illumination scenarios but removing the preamplifier and attenuators. The results are shown in figure 24.

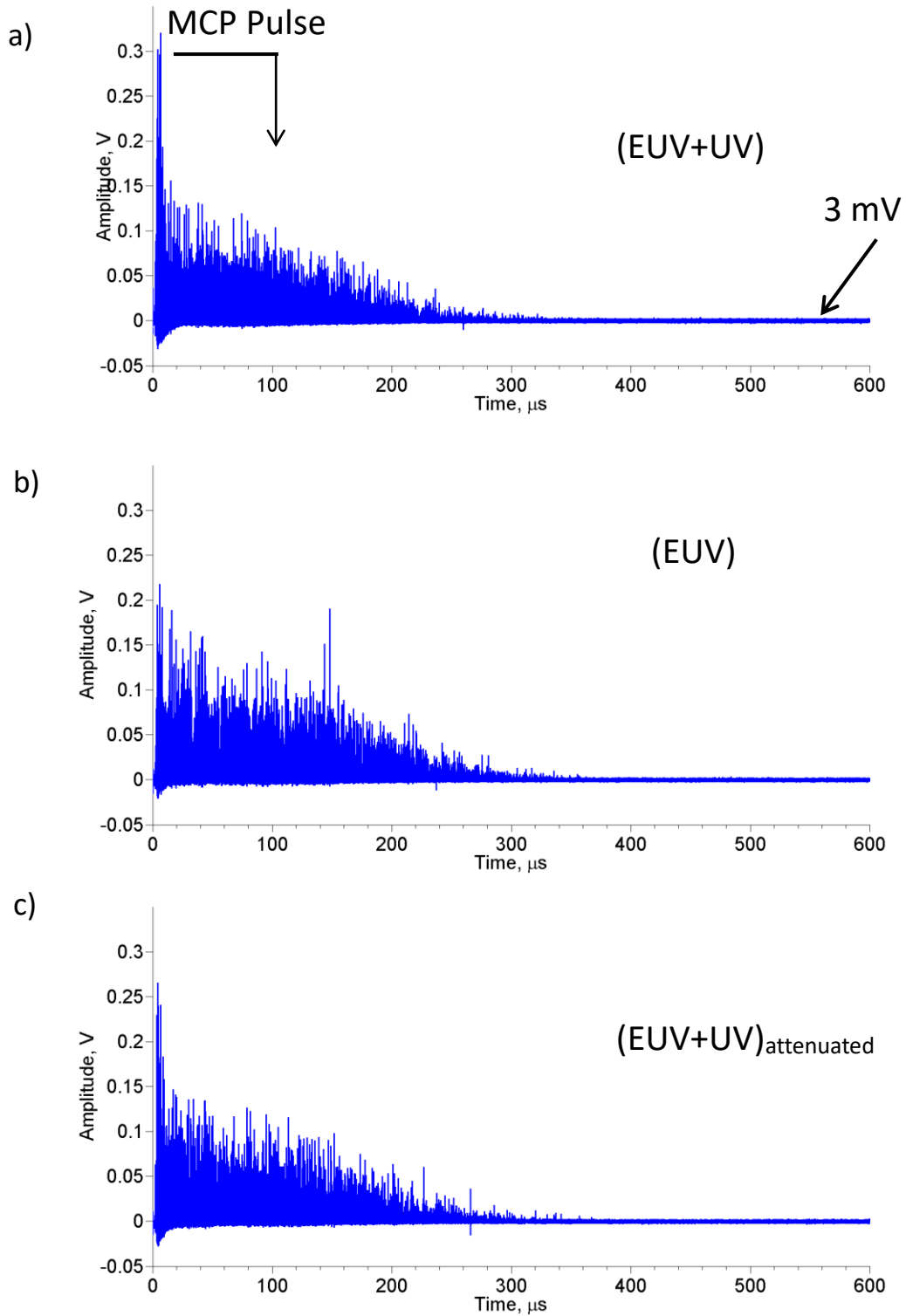


Fig. 23: Single-shot signals from the MCP using 20x preamplifier and 4.4x attenuator collected for 600 microseconds. (a) Using full intensity unfiltered EUV beam. (b) Using Al-filtered beam. (c) Using attenuated, unfiltered beam. These are the conditions at which spectra are acquired. The MCP was pulsed for 100 μ s.

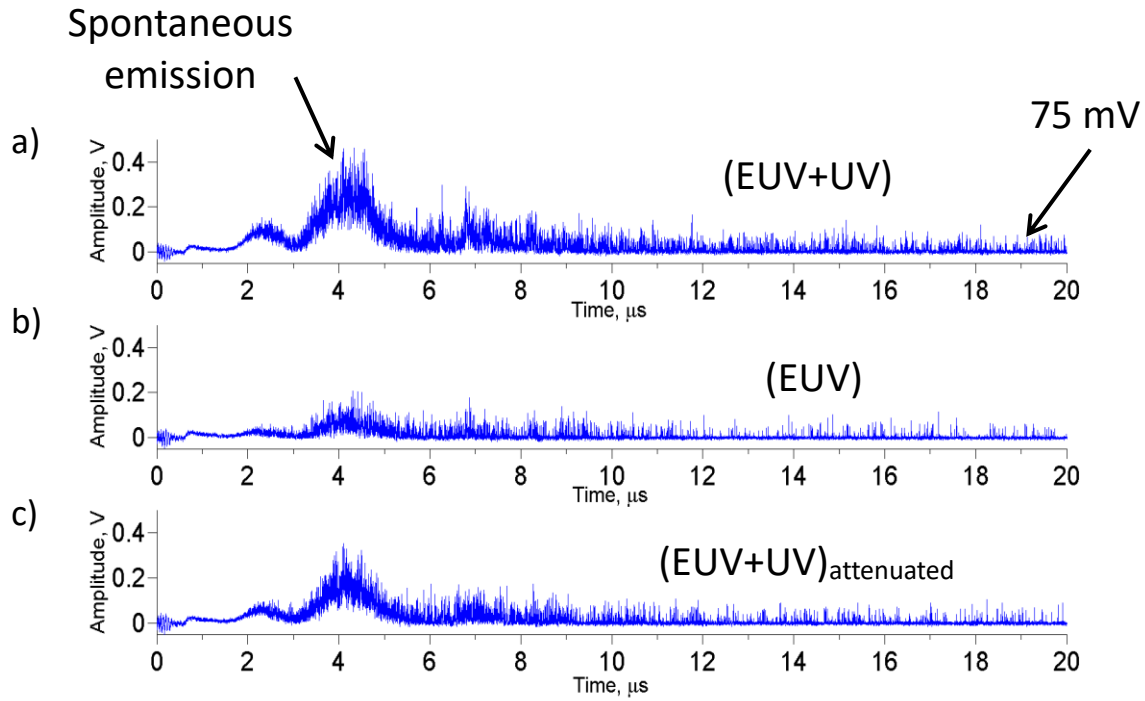


Fig. 24: Single-shot signals from the MCP collected without using the preamplifier or attenuators. (a) Using full-intensity unfiltered EUV beam. (b) Using Al-filtered beam. (c) Using attenuated, unfiltered beam. At 20 μ s, noise level is still at 75 mV.

The signal shown in figure 24a has a pronounced bump at the 4 μ s marker. This bump is missing in figure 24b, but reappears in 24c. This leads to the conclusion that this small bump is caused by UV spontaneous emission radiating from the capillary.

To rule out an electrical response from the attenuators or preamplifier that would cause the ramp noise in figure 23, testing was repeated without an aluminum filter for different combinations of the electrical attenuators and the preamplifier. The results are shown in figure 25 as signals that are not normalized in order to highlight the differences in attenuation.

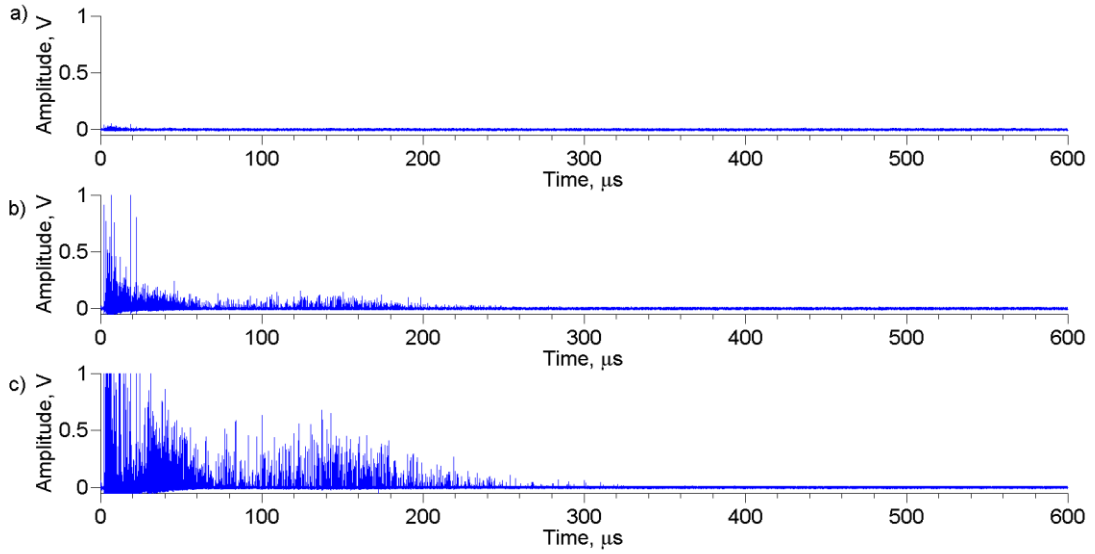


Fig. 25: Single-shot, un-normalized signals collected using different combinations of attenuators and the preamplifier. (a) Using the 20x preamplifier and two 10x attenuators. (b) Using the 20x preamplifier and a 10x attenuator. (c) Using the 20x preamplifier and a 4.44x attenuator. These settings are typical for sample analysis.

The results in figure 25 show that the ramp noise signal is dependent on the attenuation along the cable. It appears that the noise is almost absent in figure 25a, but this is because the signal is heavily attenuated and drops below the minimum background level. Since the ramp noise is dependent on the attenuation along the cable, we can conclude that this noise is generated at the MCP. This also shows that the minimum background level is invariant to the electrical attenuators and is most likely thermal noise in the electronics and computer. The spectra from the linear and reflectron MCPs were compared while keeping voltages across ion optics and the positions of motors identical. The results are shown in figure 26.

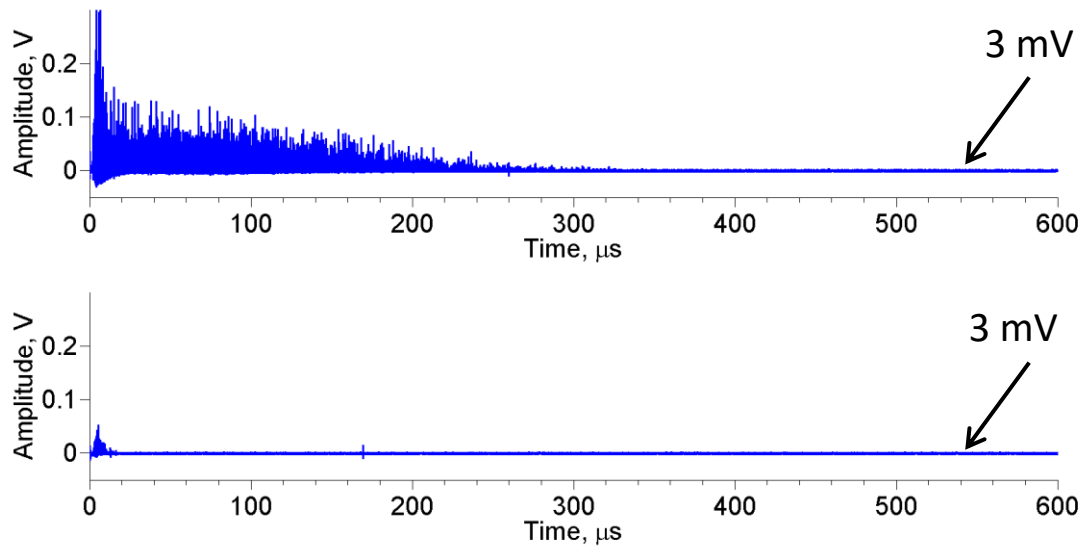


Fig. 26: Single-shot signals collected in identical conditions using the reflectron (a) and linear (b) MCPs. The signals were collected using a 20x preamplifier and 4.44x attenuator. No filter or attenuation was used.

Surprisingly, the linear MCP does not experience the same elevated noise level that the reflectron MCP does. Each MCP uses the exact same trigger box and voltage divider, and the only difference in their structure is the diameter of their active area. This suggested that a signal was causing a response in the reflectron MCP.

The next step in the diagnostic process was to determine the cause of the signal response demonstrated in figure 23. This was accomplished by tilting the first toroidal mirror laterally such that the EUV laser beam moved across the aperture near the gate valve. The behavior of the pulse seen around 16 μ s and background ramp noise as the beam is moved across the aperture is shown in figure 27.

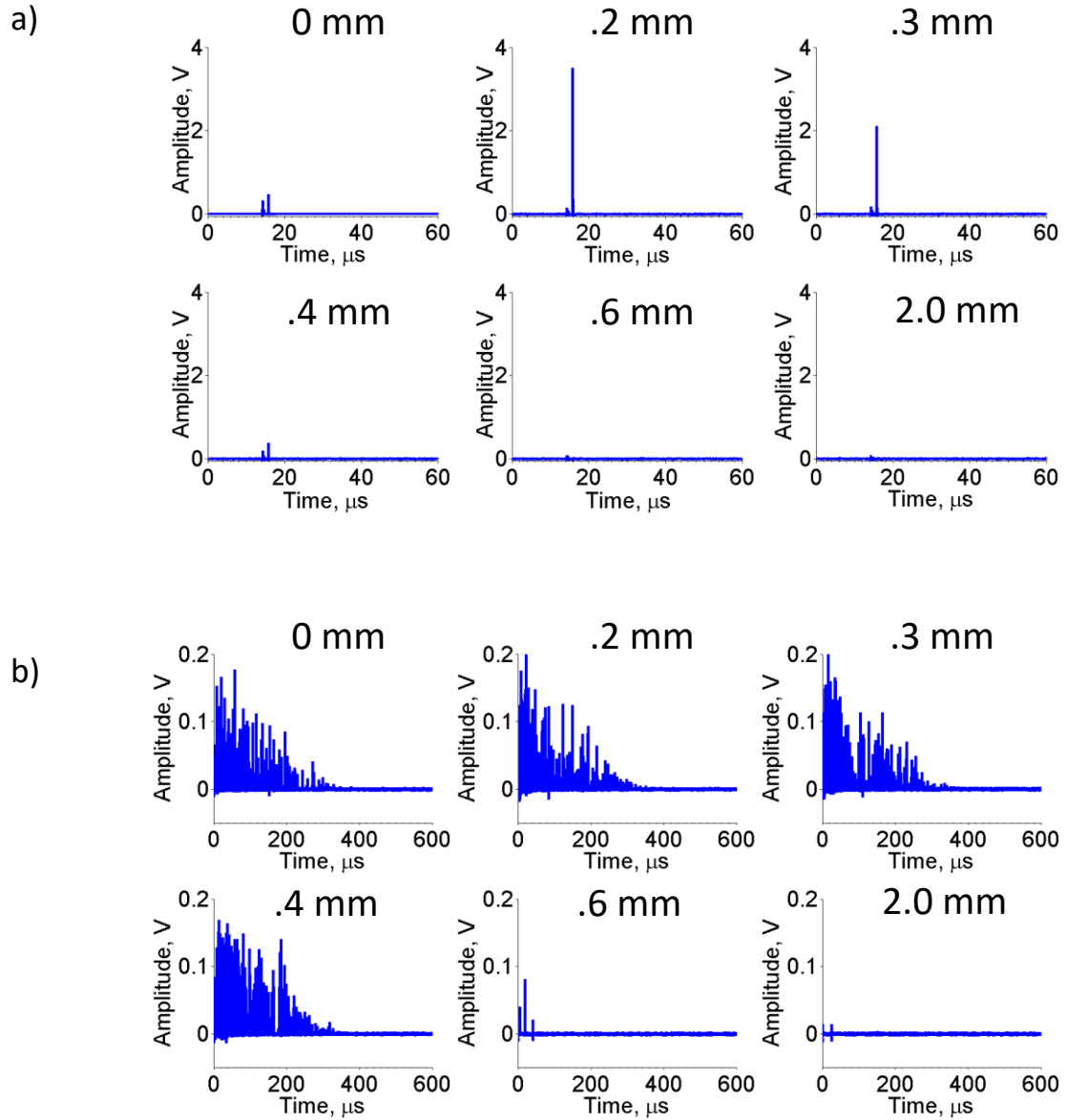
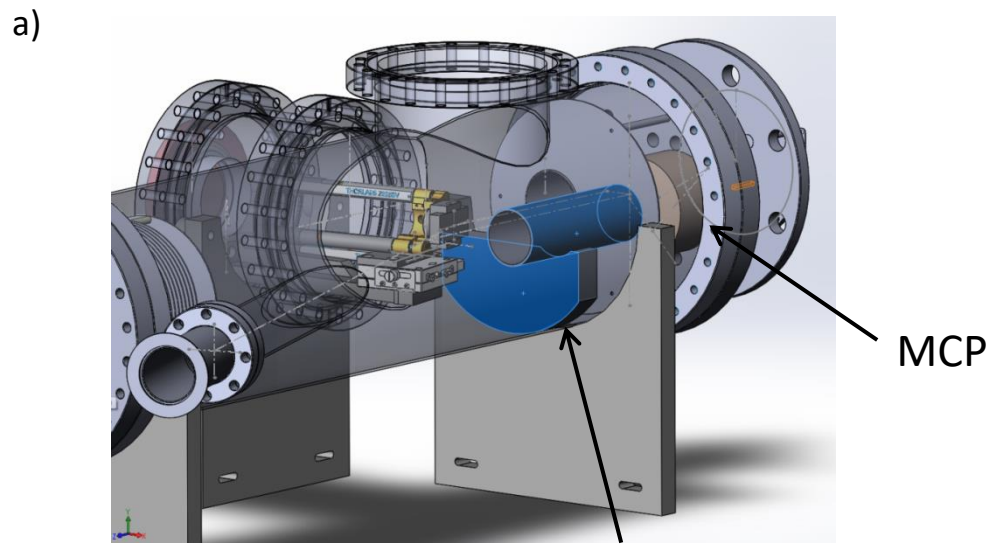


Fig. 27: (a) Spectra showing an intense pulse at $16 \mu\text{s}$ when data is acquired on from the MCP beginning $16 \mu\text{s}$ (a) and the noise background obtained (b) as the EUV beam moves across the aperture. 27a was acquired with the MCP at 1400 V in DC mode with acquisition starting $16 \mu\text{s}$ prior to EUV pulse generation. 27b was acquired by pulse-gating the MCP at 2200 V , the same conditions used when collecting mass spectra. The distance increments are determined by how far the Thorlabs motor that was tilting the mirror moved.

Figure 27 demonstrates that the pulse occurring at 16 μ s on the MCP, appearing before ions are collected, is directly correlated to whether background noise appears on the signal. Since the laser and TOF chamber are connected and open, this result rules out radio-frequency electromagnetic waves as the cause of the pulse arriving at 16 μ s or the cause of the background noise. This shows that when the EUV laser beam enters the chamber, background noise occurs. The pulse at 16 μ s has a FWHM of ~2ns. We speculate that this signal on the plot originates from EUV laser photons reaching the MCP. The number of photons interacting with the MCP is so large that it causes a massive electron avalanche and saturates the MCP. The build-up of electrons and subsequent dissipation gives rise to the background noise. Once the MCP is activated, those charges dissipate over the course of 300-400 μ s in a linearly decaying fashion.

Given the geometry of the TOF chamber, the most likely area in which EUV light could be scattered into the MCP is from the toroidal mirror in the TOF chamber. To fix this, a 6" stainless steel pipe was installed along the line of sight of the MCP to block scattered EUV photons from the mirror. The schematic of the installation and signals acquired with and without the tube are shown in figure 28. By comparing figure 28b and c, it is apparent that the noise signal has decreased slightly but the bulk of the noise signal is still present. This suggests that the EUV beam is scattering off of some other components and is still travelling down the pipe.

After a closer look at the 16 μ s pulse in figure 19a, it appears that the pulse is made up of two pulses 6 ns apart, as shown in figure 29. The second pulse is ~40x larger than the first.



Pipe
Assembly

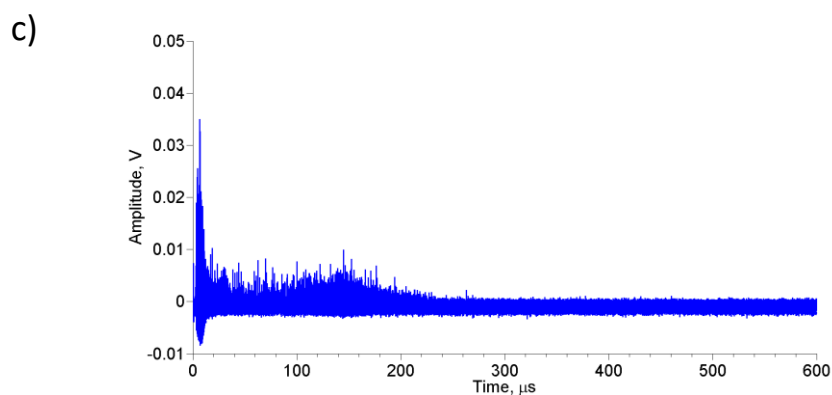
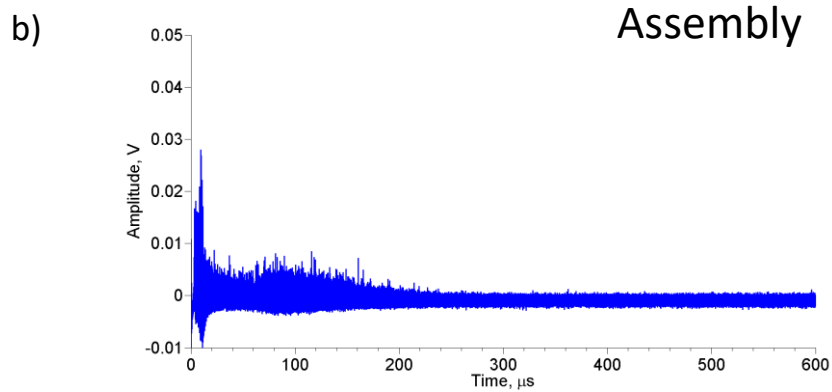


Fig. 28: (a) A schematic showing how and where the pipe was installed. (b) A noise signal acquired before the pipe was installed. (c) A noise signal acquired under identical conditions after the pipe had been installed.

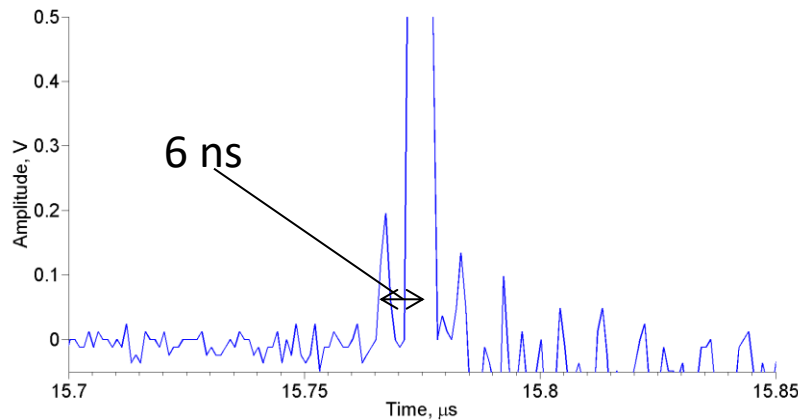


Fig. 29: The pre-pulse shown up close showing that it is composed of two pulses 6 ns apart from one another.

A 6 ns delay between two, 2-ns-FWHM peaks caused by EUV light is equivalent to the second peak traveling a distance of 1.8 m. If it is assumed that the first, smaller peak, is caused by the EUV laser traveling directly toward the MCP, then the second, more intense peak must be reflecting off of components in the TOF chamber and traveling an additional 1.8 m.

To isolate the origin of the reflected peak in figure 29, we displaced the metallic zone plate that is on the EUV beam path. The signal that was obtained by moving the zone plate position in 1-mm increments along the x-axis is shown in figure 30. The results of figure 30 show scattered EUV photons that are reaching the MCP are reflecting off the zone plate. At first this scenario seems unlikely as 46.9 nm light is highly absorptive, but the MCP operating at 2200 V is also a very sensitive detector. The reflectance at normal incidence of silicon at 46.9 nm is ~0.05%, which is what the zone plate holders are made of, and ~5% for stainless steel which is what the chamber is made out of.

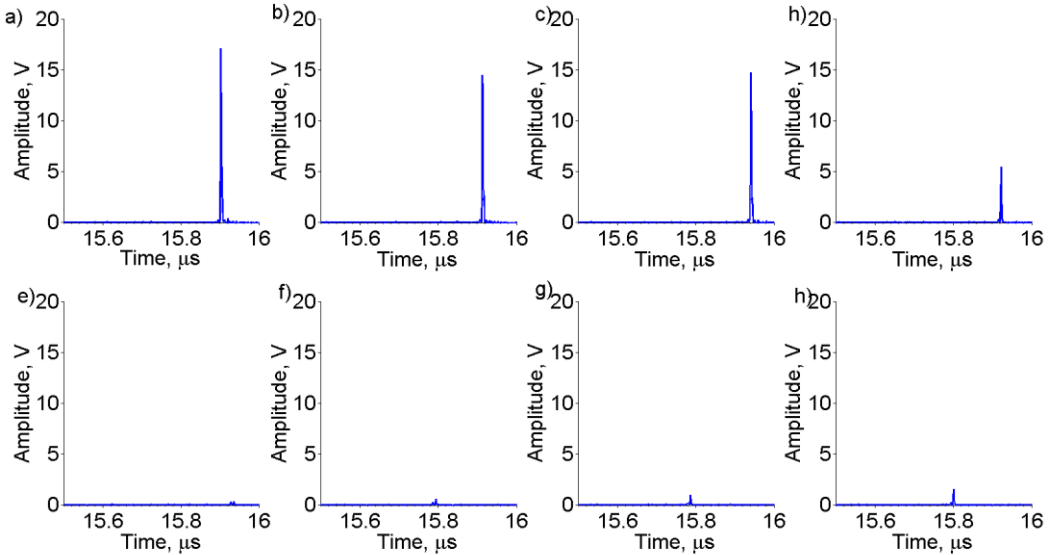


Fig. 30: The behavior of the pre-pulse as the zone plate is moved laterally. (a) Zone plate at normal position. (b) Zone plate moved 1 mm. (c) 2 mm. (d) 3 mm. (e) 4 mm. (f) 5 mm. (g) 6 mm. (h) 7mm.

Even if 10^{12} photons are reflected off of the zone plate holder and scattered twice off of the chamber walls, 10^6 photons would still be reaching the MCP, more than enough to cause extensive charge buildup on the detector. The signal reflecting off of the zone plate would need to travel ~ 1.8 meters to reach the MCP, which would account for the 6 ns delay between peaks as seen in figure 29. This means that the first, smaller peak to arrive is traveling directly into the MCP, most likely by the EUV beam diffracting off the edges of the aperture and scattering off the tube and into the MCP.

In summary, the observed elevated background noise is due to scattered EUV photons reaching the MCP and creating a charge buildup that then decays for ~ 300 μ s. When the detector is activated, it discharges similar to a capacitor. The RC constant of the detector cannot be easily modified since the resistance of the cables is 50Ω and the overall capacitance

of the detector is \sim 70 pF. Therefore, the best method for eliminating the background noise would be to prevent the EUV scattered photons from interacting with the detector.

3.2 Noise Mitigation

The noise due to cable reflections had been eliminated early on in the diagnostic process. All that remained were the pulses at 16 μ s due to EUV light and the background signal that was found to be caused by these intense pulses. Figure 29 indicates that two separate groups of EUV scattered photons are interacting with the MCP detector: one travelling directly into the detector, and the other reflecting off of the zone plate and scattering off of the chamber walls.

A solution to mitigate the background noise due to the first EUV peak would be to prevent the EUV beam from diffracting off of the aperture as the beam enters the TOF chamber. One potential solution is to simply increase the diameter of the aperture such that the beam no longer interacts with it. The aperture was previously designed with a 4 mm diameter to assist with differential pumping and prevent the turbo pump in the TOF chamber from getting overloaded when the gate valve is opened and pressure equalizes. Over the years, it has been found that the pressure difference when opening the gate valve is not a big issue, so the aperture could be enlarged to a 5-6 mm diameter without causing an issue.

To eliminate the other EUV peak that likely results from EUV photons reflected off the zone plate, the solution would be to install a conical beam blocker possibly made out of aluminum or another conductive, lightweight material, and coated with resist. Actively blocking scattered EUV photons would improve signal-to-noise and enable detection of trace elements

with $\sim 10x$ less averaging than is currently done. A cross-section of the conical beam blocker and zone plate holder is shown schematically in figure 31.

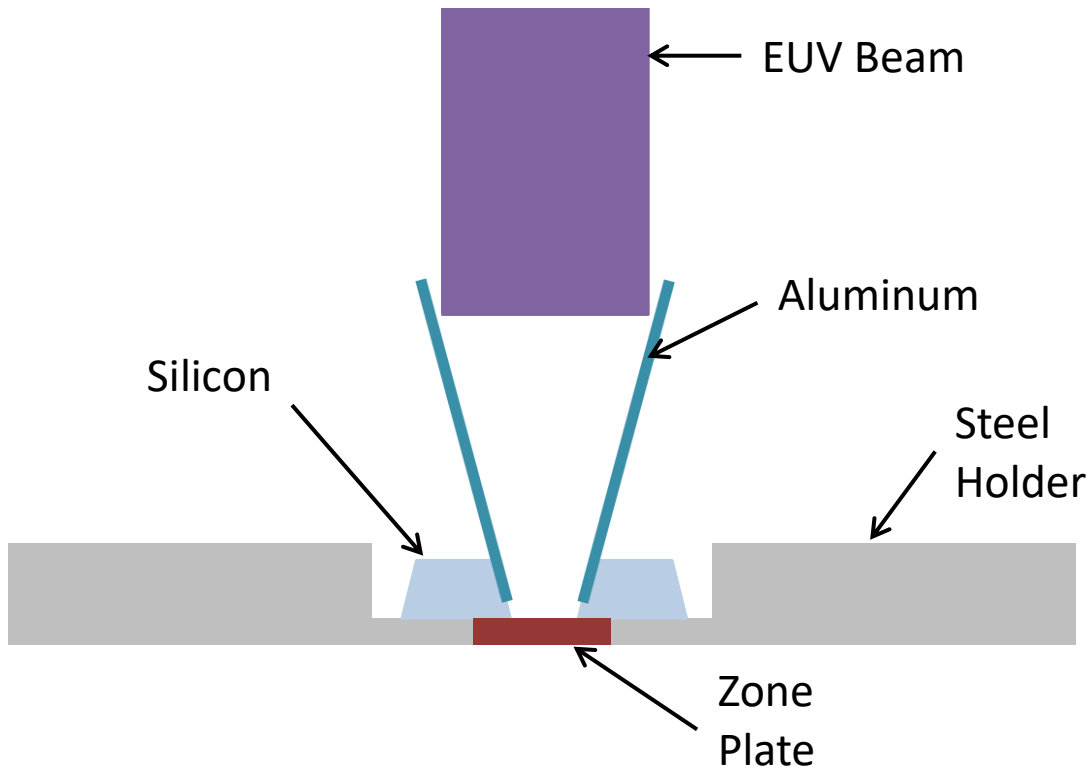


Fig. 31: A top down cross-section diagram showing the zone plate, holder, and aluminum beam blocker to be installed.

The idea of the beam blocker is that the EUV beam will reflect off of the blocker at an angle such that it will not be reflected directly backwards. The blocker has to be conductive so that when the EUV beam generates charges on the blocker, the charges can dissipate easily.

If these solutions are put in place, then both peaks shown in figure 29 caused by the EUV scattered photons should be eliminated, thus eliminating the background noise.

Chapter 4: Mass spectrometry Analysis and Imaging of Trace Elements and Actinides

4.1 Introduction

This chapter describes the results of experiments designed to detect trace amounts of actinides and achieve nanoscale lateral resolution imaging on uranium oxide particles by EUV TOF. Some of the current analytical techniques that are capable of elemental composition mapping include atom probe tomography (APT) and scanning transmission electron microscopy energy dispersive x-ray spectrometry (STEM-EDX), as well as SIMS and LA-ICP-MS. These systems cover a wide range of spatial resolutions and sensitivities, but each technique is useful in atomic analysis in its own way.

The goal of EUV TOF is to maximize both spatial resolution and sensitivity to provide an instrument that can achieve nanoscale resolution and sensitivities ranging from 10-100 ppm. EUV TOF is similar to LA-ICP-MS in that a laser is used to ablate a target material, the main difference being that EUV TOF does not require an external ionization method, similar to SIMS. 46.9 nm light can also be focused down to spot sizes of 100 nm, which is similar with SIMS TOF and nanoSIMS. Given these similarities to SIMS, several of the following results are compared to results from a TOF.SIMS5 IonTOF instrument operated at PNNL by collaborators. The results are divided into four sections: The trace element analysis on NIST glasses, the sample utilization efficiency measurements, the lateral resolution measurements, and the uranium oxide imaging application.

4.2 Trace Analysis

Figure 32 shows the mass spectra collected from the four NIST glasses 611-617 with EUV TOF. These spectra are each the result of a $10 \mu\text{m} \times 10 \mu\text{m}$ crater being formed with 1,200 laser pulses on each glass sample. Data were collected from each pulse and averaged together. For comparison, the spectrum in figure 21a was collected with a single laser shot.

Figures 32a and b show several intense peaks that represent the composition of the glass. Figure 32b has several molecular peaks labeled with a likely molecular ion, however these are not definitive. The only non-substrate mass peaks in the first two panels are rubidium and cesium. Any weakly present isotopes in those mass ranges would not appear in this spectrum due to the limited dynamic range of the MCP. Rb and Cs have the lowest ionization potentials of any stable isotope in the periodic table, so they are efficiently ionized by the EUV pulse. Figures 32c and d no longer include matrix peaks, so various trace isotopes doped in the glasses are able to be detected from NIST 611 and 613. Since trace isotopes are not observed for NIST 615 and 617, the nominal concentration of 50 ppm for NIST 613 is probably near the detection limit for EUV TOF. Some of the mass peaks in panel c are asymmetric and noisy. This could be due to matrix interferences occurring at similar masses, or it could be the result of timing irregularities due to the charging of the substrate. A higher mass resolution would be needed to determine specifically why the asymmetry occurs. Figure 33 shows a mass spectrum comparison between EUV TOF and SIMS TOF after analyzing the same amount of material of NIST 611. The EUV TOF data in figure 33 is a repeat of the data shown in figure 32.

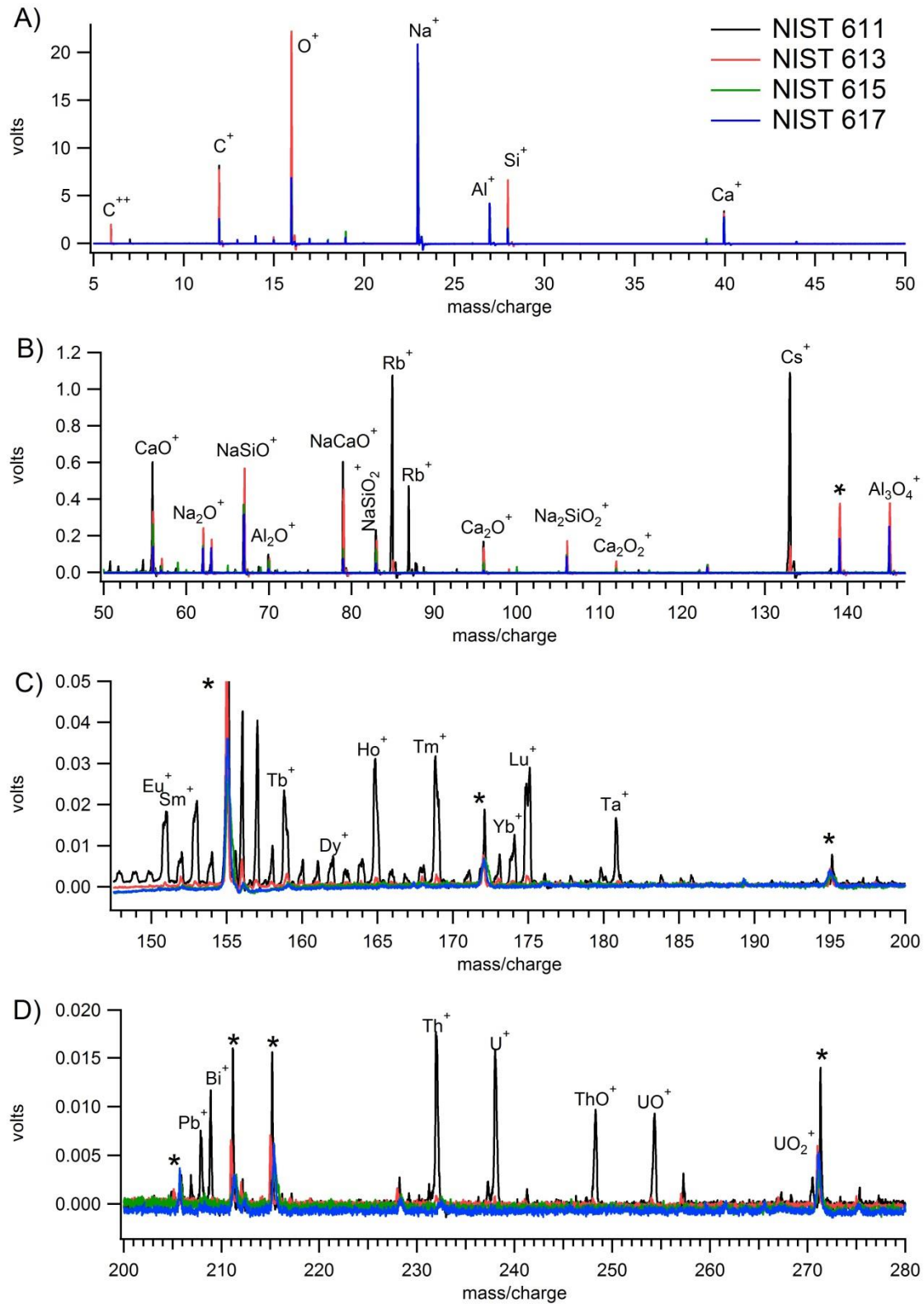


Fig. 32: A waterfall plot showing the mass spectra of NIST 611, 613, 615, and 617 up to 280 Daltons. The peaks labeled with an asterisk are unidentified. The plots are separated by mass range.

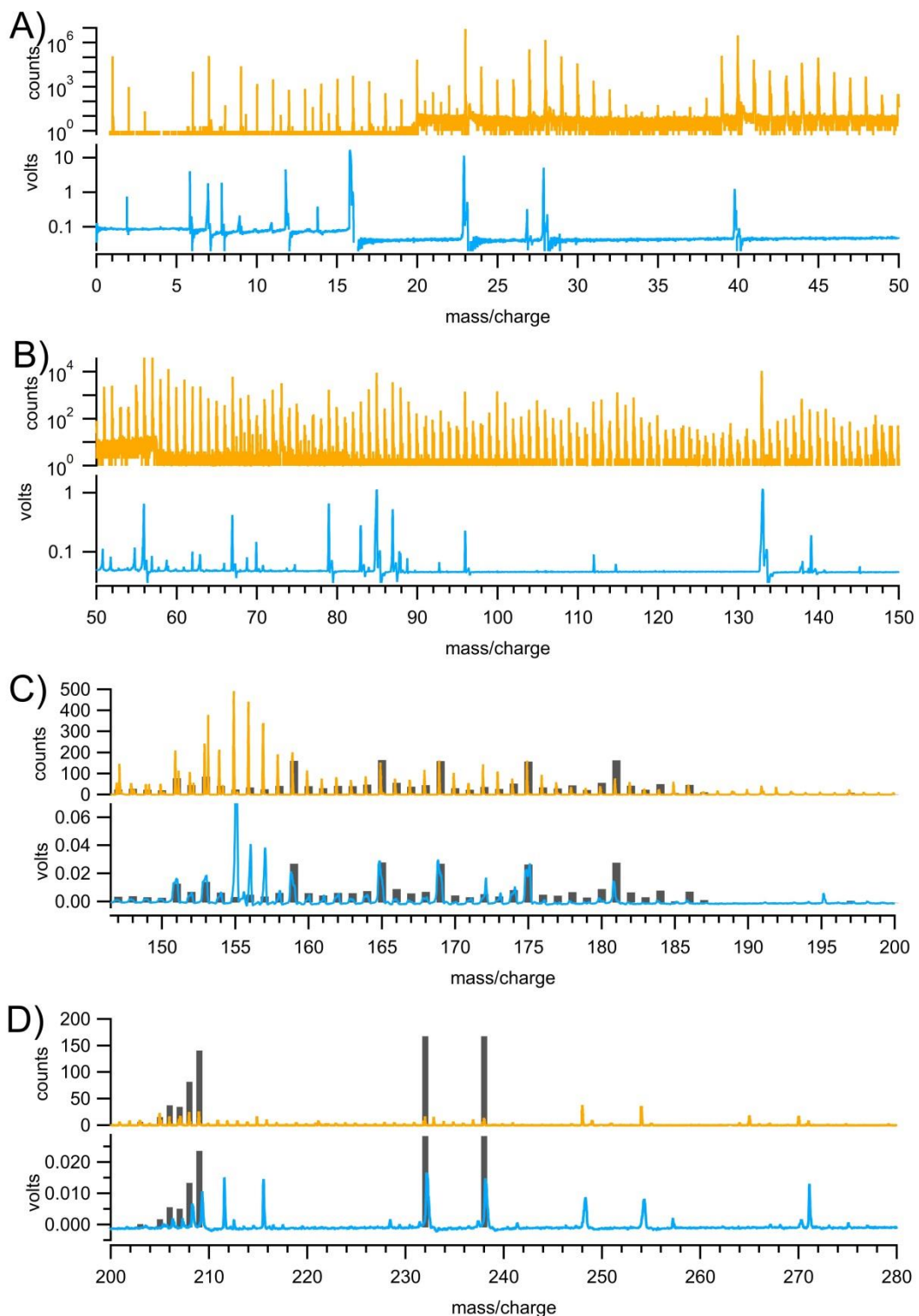


Fig. 33: A comparison of SIMS TOF and EUV TOF mass spectra from NIST 611 glass. The SIMS TOF spectrum is represented in orange and EUV TOF in blue. The black bars represent calculated signal intensities for NIST 611.

The goal of comparing SIMS TOF and EUV TOF is to help standardize the data produced by EUV TOF and determine how the data should be considered in the larger field of analytical mass spectrometry. It also helps in determining what limitations are inherent to the individual sources and what limitations could be shared by both instruments since both use TOF mass analyzers. The first two panels use logarithmic scaling due to the large intensity differences of the matrix components being detected, while the last two panels are able to fit on a linear plot since the differences between peaks is less dramatic. The EUV TOF has far less molecular interferences than SIMS TOF in the whole mass range. While EUV TOF has sporadic and intense molecular peaks that arise every so often, the SIMS TOF spectrum shows a mass peak on nearly every integer mass. This is most likely due to the difference between the sputtering and ablation process⁷⁰. The calculated black bars for uranium and thorium are set at the same level for both techniques so the comparison in figure 33d is comparable. The main conclusion from figure 33c is that both techniques agree well for the rare earth range of mass peaks. In 33d, EUV TOF is noticeable more intense for Tl, Pb, and Bi, as well as U, and Th. Both techniques show UO and ThO peaks clearly. Since EUV TOF has fewer interferences than SIMS TOF in the high mass range, the EUV source will be beneficial when attached to a magnetic sector instrument for high mass resolution isotopic analysis. Figure 34 compares a mass spectrum collected with EUV TOF with one taken on a dynamic SIMS instrument.

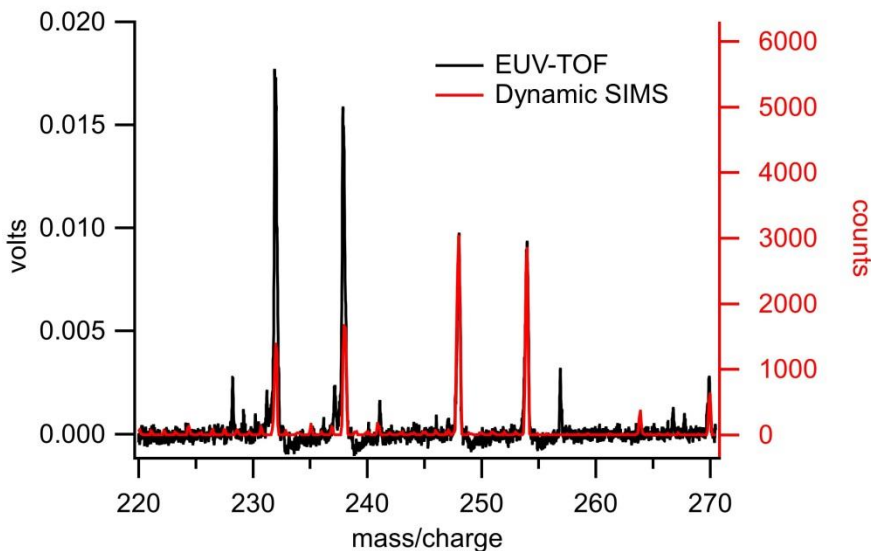


Fig. 34: The same EUV TOF mass spectrum data as shown in figures 29 and 30 represented in black, compared with dynamic SIMS data in red.

The mass spectra in figure 34 are normalized with respect to the UO and ThO peaks. In this comparison, the isotope peaks are much more intense in the EUV TOF spectrum than in dynamic SIMS. This is most likely due to dynamic SIMS's primary O⁻ ion beam since it would add many more oxygen atoms into the sputtering process and promote the formation of additional oxide molecules. It can be difficult and time consuming in SIMS to select primary ions that will affect molecular fragmentation, but as shown in Figure 35, EUV TOF has the ability to tune the amount of fragmentation that occurs through laser attenuation. Figure 35a is composed of four spectra, each averaged over 1,200 laser pulses at different laser pulse energies. Figure 35b is a representation of a Riemann sum taken under the peaks of figure 35a and plotted versus pulse energy.

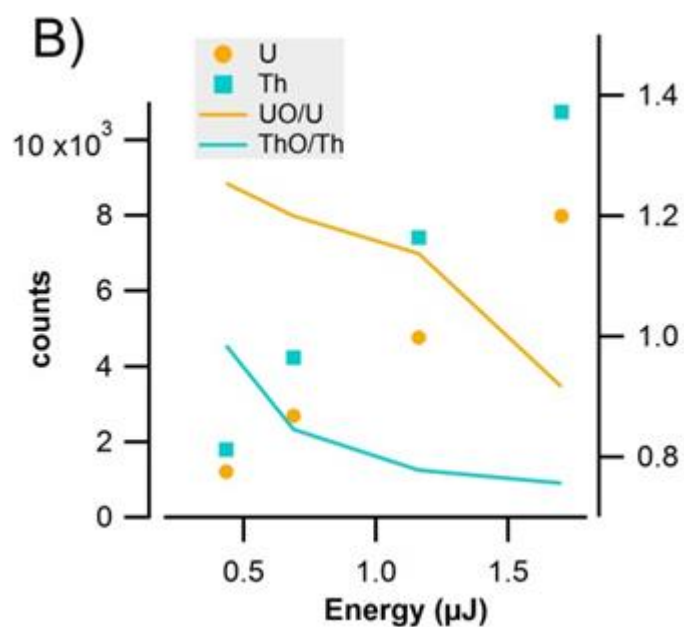
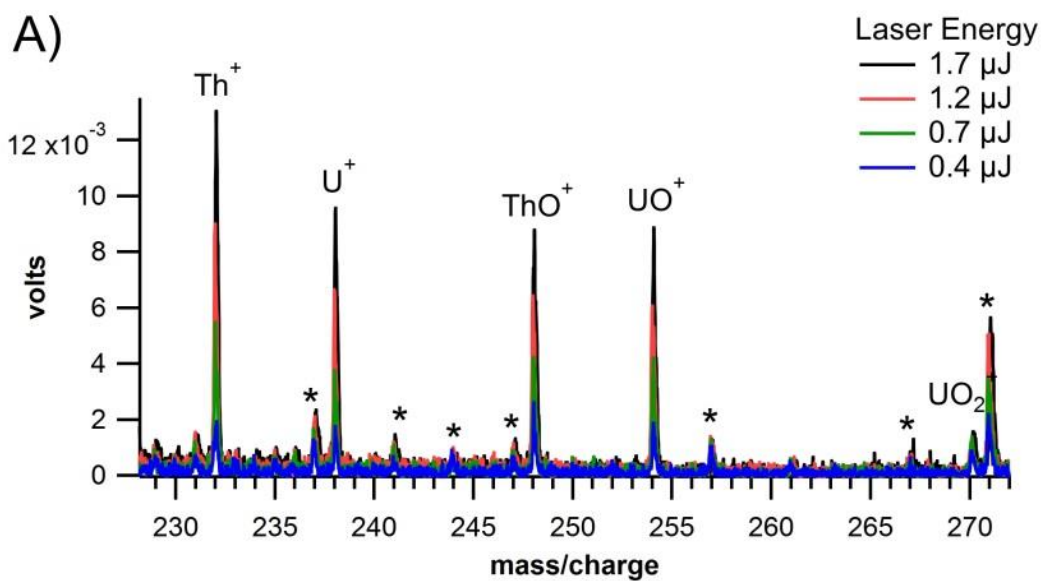


Fig. 35: (a) Four mass spectra taken on NIST 611 glass at different laser pulse energies. (b) The integral of each curve and the oxide-to-element ratios plotted versus pulse energy.

Figure 35a demonstrates that as laser pulse energy is reduced, all of the mass peaks are reduced in intensity. However, the elemental peaks reduce faster than their corresponding oxide peaks and the ratio of oxide-to-element ions is increased, as shown in figure 35b. The laser pulse energy and intensity change the properties of the plasma in which the ions are formed, and this influences the distribution of atomic and molecular ions in the plasma.

4.3 Sample Utilization Efficiency

Figure 36 shows the sample utilization efficiency (SUE) measured with uranium atoms using the same data set as in figure 35. The calculated efficiency is the average calculated over the four different averaged spectra collected using different pulse energies.

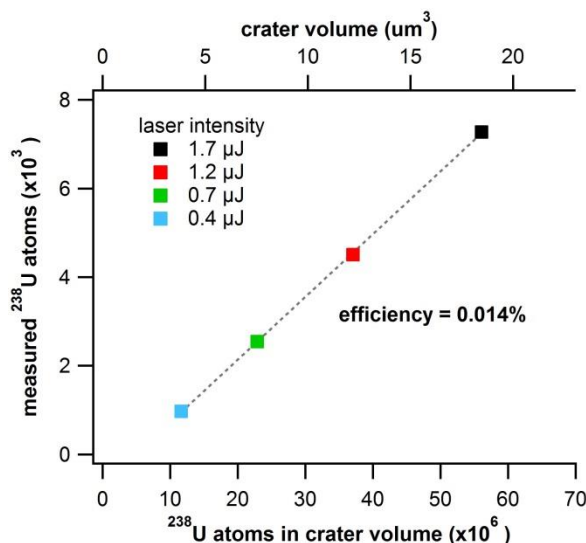


Fig. 36: The efficiency of detecting uranium ions calculated for four separate crater volumes and laser energies. The stated efficiency is the average slope of the four measurements.

For uranium, this was calculated to be 0.014% and for thorium it was 0.017%. As a comparison, SIMS TOF ablated a volume roughly equivalent and calculated an SUE for uranium which was 0.013%. These results are almost the same and could indicate a limitation due to the detection scheme. The SUE's for rubidium and cesium couldn't be directly measured due to a delay on turning on the MCP. This delay is meant to keep intense peaks from being detected, thereby enhancing the sensitivity available to the detector for the mass peaks of interest. However, the SUE's for rubidium and cesium were estimated by taking the calculated value for SUE for uranium and proportionalizing it to cesium. This was done by using the equation

$$SUE_{CS} = SUE_U * \frac{C_U}{C_{CS}} * \frac{I_{CS}}{I_U} * \frac{M_{CS}}{M_U} \quad (4-1)$$

Where:

- I_U is the intensity of uranium in a 4-by-4 data collection
- I_{CS} is the intensity of cesium in the same data set
- C_U and C_{CS} are the concentrations of the elements found in NIST 611
- M_U and M_{CS} are the molar weights of the isotopes

The equation calculates the SUE as 1.55%, and a similar value is given for rubidium.

Since this is only an estimation, we can only say with reasonable confidence that the measured SUE should be above 1%. It is reasonable to speculate that percent level SUE of U and Th could be obtained with an EUV laser for ablation and ionization with a more efficient magnetic sector instrument for mass analysis. An image of the overlapping crater scan is shown in figure 37.

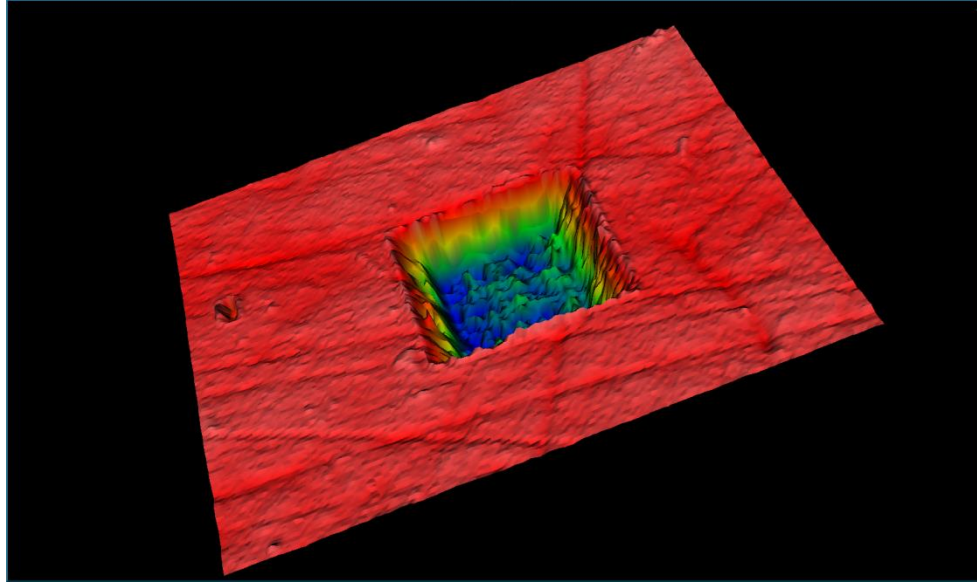


Fig. 37: A 3D model of an ablated volume generated from a White Light Interferometer scan. This crater was created with an EUV beam energy of $1.2\mu\text{J}$ per pulse.

4.4 Lateral Resolution

The EUV TOF is specifically designed for composition imaging. In previous work, we showed the method can map the distribution of organic molecular components with a lateral spatial resolution of 75 nm and a depth resolution of 20 nm. Composition mapping is implemented by displacing the specimen across the focused EUV laser beam. The highest lateral spatial resolution is obtained by attenuating the laser fluence to reduce the diameter of the ablated spot to values at which the ion peaks are 5 \times the noise floor in the mass spectrum. We employed the same methodology as with organics to evaluate the lateral resolution of EUV TOF for composition mapping of inorganic samples. The sample used for this experiment consisted of a comb of nickel lines 1 μm wide and 100 nm thick (Figure 38a).

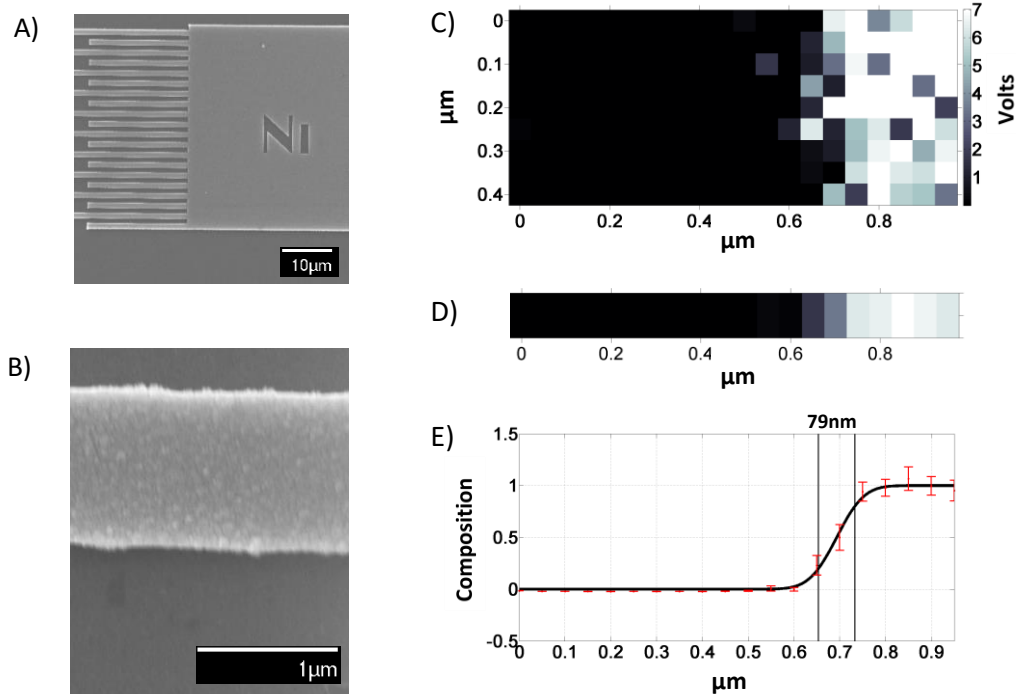


Fig. 38: Lateral resolution assessment. (A) Scanning electron microscope (SEM) image of the nickel comb structure. (B) SEM image of a single nickel line. (C) Composition image comprised of 9 adjacent passes from substrate on the left to Ni on the right depicting the distribution the main Ni isotope. (D) Column-averaged data. (E) Normalized column-averaged data fitted with an error function and showing the 20-80% distance corresponds to 80 nm.

The lines are sharp and well defined as shown in Figure 38b. The line edge roughness (LER) was measured on an SEM image by detecting the 50% point on the nickel edge over a distance of 2.5 μm along the edge. The LER is calculated to be 29 nm by finding the 3σ of the collected data points along the edge. The sharpness of the edge was measured using the SEM image of Figure 38b by finding the average distance between the 20% and 80% intensity change across the edge averaged over a 2.5 μm distance along the edge. The edge sharpness was calculated to be $21 \text{ nm} \pm 4 \text{ nm}$.

Figure 38c shows the distribution of the major isotope of Ni at 58 Da on a region near an edge of a Ni line in the comb. This composition image was obtained from the analysis of mass

spectra resulting from the ablation of the sample in the form of a 9 by 20 grid in which the step size is 50 nm. It is then averaged along one direction to form the line scan shown in Figure 38d. These data points are plotted, normalized, and are fitted to an edge spread function (ESF), which is the standard method for determining lateral resolution.

$$ESF = I_{min} + \frac{I_{max}-I_{min}}{2} \left(1 + \operatorname{erf} \left(\frac{x-\mu}{\sigma\sqrt{2}} \right) \right) \quad (4-2)$$

Where I_{max} and I_{min} are the normalized maximum and minimum mass peak intensities in the line scan.

A fit of the data of Fig. 38d using $I_{max}/I_{min}= 350$ yielded $\sigma = 47$ nm and $\mu = 0.63$ μm . The lateral resolution taken as the distance between the 20% and 80% relative intensity points on this knife-edge ESF curve is 79 nm which is very similar to previously obtained results.

4.5 Uranium Oxide Particle Imaging

Nanoscale resolution images with isotope differentiation were obtained by ablating adjacently placed, micrometer-sized uranium oxide particles with differing isotope compositions. The particle pair was first scanned with a low-resolution 10×10 pixel scan with a 0.5 μm step size, Figure 39a.

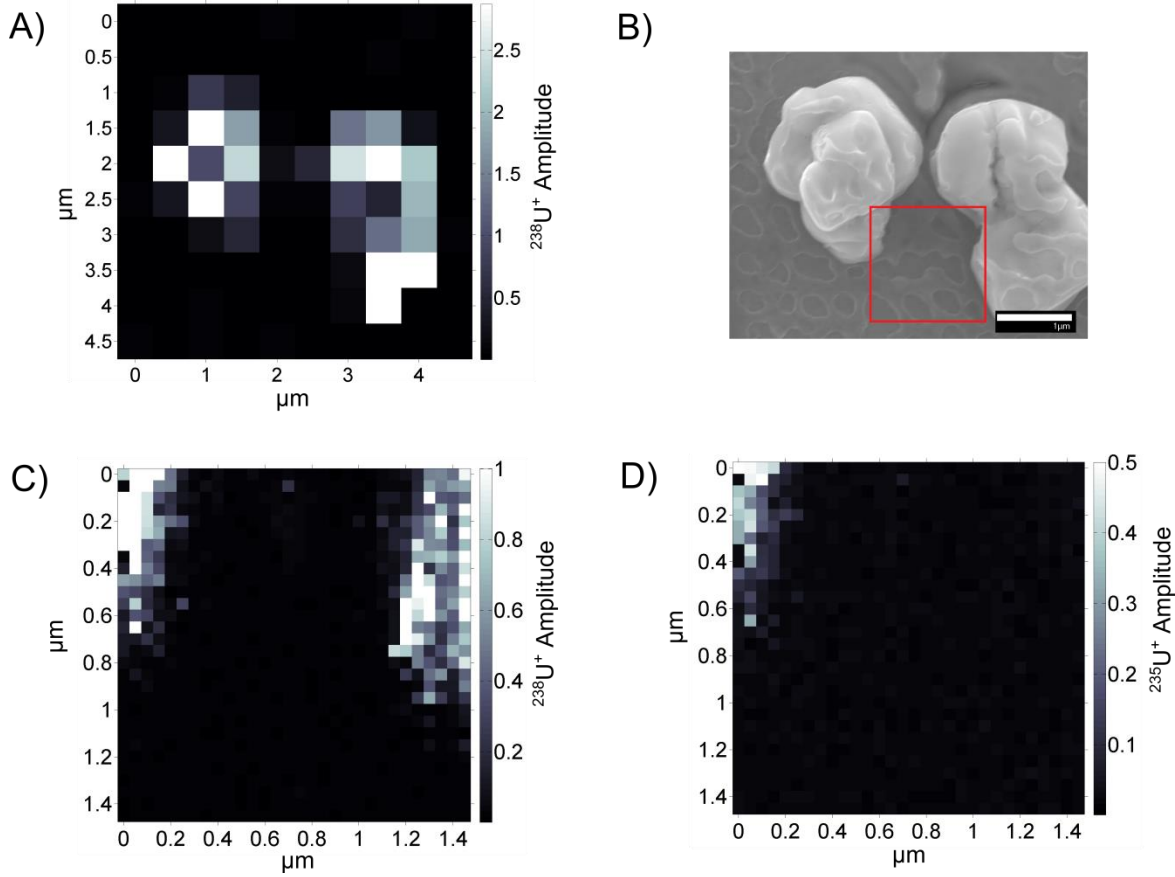


Fig. 39: Uranium oxide particle images and isotopic mapping. (A) Lower resolution mass spectral image of two uranium oxide particles generated from the ^{238}U isotope. (B) SEM image of same uranium oxide particles conducted after EUV analysis. The craters from the low resolution imaging are visible in both the particle and the substrate. The area of the high resolution EUV analysis is highlighted with the red square. (C) EUV TOF image of uranium oxide particles generated by monitoring the ^{238}U isotope signal. (D) Same area showing ^{235}U isotope. The pixel size of (C) and (D) is 50 nm.

The ablation craters left behind by this coarse scan are visible on and around the particles as shown in the SEM image, Figure 39b. A small portion of the particle pair was then scanned in a 30×30 grid pattern with 3 laser pulses per location and with a 50 nm step size. The red box in Figure 39b indicates the area where the high resolution raster took place. Figure 39c shows the averaged intensity map of ^{238}U (signal averaged over the three co-located sequential shots and the ^{238}UO and $^{238}\text{UO}_2$ peaks). This process is repeated in Figure 39d showing the corresponding image for ^{235}U and its oxides. Although the dynamic range limitations of MCPs

make it difficult to conduct precision uranium isotope analysis, an initial estimate of the ratio can be produced from the data in Figures 39c and 39d. Averaging the ratios from individual pixels from the enriched particle returns a $^{235}\text{U}/^{238}\text{U}$ ratio of 0.248 ± 0.006 evenly distributed throughout the area of the scanned particles. The expected value from the U200 standard is 0.2513 ± 0.0003 .

Chapter 5: Conclusions and Future Work

5.1 Need for sensitive mass spectrometry systems

Imaging mass spectrometry is a valuable analytical tool in a wide range of fields of science and technology. In the field of biology, highly sensitive mass spectrometers are needed to detect trace amounts of isotopes and to map the composition of micro and nanoscale structures. Most mass spectrometers are specialized such that they either have excellent resolution but poor sensitivity or vice versa. The primary method currently available that fit both criteria is SIMS TOF⁷¹ since it can image with nanoscale resolution and has ppm sensitivity. EUV TOF has similar attributes of having both high sensitivity and high spatial resolution, so SIMS TOF was a natural choice for comparison of the two techniques in chapter 4.

5.2 Conclusion from Results

The thesis work involved the collaboration with PNNL to perform experiments of trace analysis, SUE measurement, lateral resolution imaging, and mapping the composition of uranium oxide particles. This collaboration has provided the CSU group with valuable data on EUV TOF and one-to-one benchmarks on how the current iteration of the EUV TOF system compares to similar technique such as SIMS TOF. These results open up EUV TOF to new opportunities in nuclear forensics.

The diagnostic work performed for noise reduction was motivated by the need to identify U and Th isotopes doped at lower concentrations. Extensive characterization

demonstrated that the EUV pulse is scattering far more than previously thought. Despite perhaps only a thousandth or ten-thousandth of this beam's intensity reaching the MCP, a large amount of noise is created due to the MCP's high sensitivity.

5.3 Future work

There are quite a few improvements that can be made to the EUV TOF system to improve its performance for nuclear forensic applications, as well as several experiments to be performed to better characterize the technique. For further characterization, the SUE for many elements in the NIST standards should be determined, specifically rubidium and cesium. Also, while we know the sensitivity is at least 50 ppm, and maybe even better once the background noise is reduced, the specific sensitivity of the instrument would be an important metric to collect. The sensitivity, much like the SUE, is isotope dependent.

Improvements on the system itself include automating the attenuation pressure to stay constant over time, incorporating the Stanford delay generator that sets the delay of the MCP into the LabVIEW imaging program, machining a new spark gap for the capillary to reduce the time spent during maintenance. For noise reduction, the beam can be blocked from entering the tube surrounding the MCP opening by blocking a portion of the tube, or possibly extending the tube. A piece of non-reflective material such as plastic could be used to prevent scattering off of the zone plate.

The results of chapter 4 conclusively show that EUV TOF is already quite competitive in the analytical mass spectrometry landscape and could surpass similar methods as the instrument becomes more developed.

Bibliography

1. Hoffmann, E. de & Stroobant, V. *Mass Spectrometry: Principles and Applications*. (1996).
2. Herzog Viehböck, F. P., R. F. K. Ion Source for Mass Spectrography. *Phys. Rev.* **76**, 855 (1949).
3. Hillenkamp, F., Karas, M., Beavis, R. C. & Chait, B. T. Matrix-assisted laser desorption/ionization mass spectrometry of biopolymers. *Anal. Chem.* **63**, 1193A–1203A (1991).
4. Kuznetsov, I. *et al.* Three-dimensional nanoscale molecular imaging by extreme ultraviolet laser ablation mass spectrometry. *Nat. Commun.* **6**, 6944 (2015).
5. Fernández, F. M. *et al.* Hadamard transform time-of-flight mass spectrometry: A high-speed detector for capillary-format separations. *Anal. Chem.* **74**, 1611–1617 (2002).
6. Wolff, M. M. & Stephens, W. E. A pulsed mass spectrometer with time dispersion. *Rev. Sci. Instrum.* **24**, 616–617 (1953).
7. Tissue, B. M. Time-of-Flight Mass Spectrometry (TOF-MS). (2000). Available at: <http://www.tissuegroup.chem.vt.edu/chem-ed/ms/tof.html>.
8. Liebl, H. *Applied charged particle optics. Applied Charged Particle Optics* (2008). doi:10.1007/978-3-540-71925-0
9. Mamyrin, B. A., Karataev, V. I., Shmikk, D. V & Zagulin, V. A. The mass-reflectron, a new nonmagnetic time-of-flight mass spectrometer with high resolution. *Sov. Phys. - JETP* **37**, 45–48 (1973).
10. Khan, O. Mass Analyzers (Mass Spectrometry). *LibreTexts* (2015). Available at: [https://chem.libretexts.org/Core/Analytical_Chemistry/Instrumental_Analysis/Mass_Spectrometry/Mass_Spectrometers_\(Instrumentation\)/Mass_Analyzers_\(Mass_Spectrometry\)](https://chem.libretexts.org/Core/Analytical_Chemistry/Instrumental_Analysis/Mass_Spectrometry/Mass_Spectrometers_(Instrumentation)/Mass_Analyzers_(Mass_Spectrometry)).
11. Kentucky, U. of. Summary of the characteristics of different mass analyzers General : The effect of electromagnetic fields on ions.
12. Magnetic -Deflection or Sector Mass Analyzer. *Organic Spectroscopy* (2011). Available at: <http://orgchemguide.blogspot.com/2011/04/magnetic-deflection-or-sector-mass.html>.
13. Dodds, A. J., Pollock, E. M. C. & Land, D. P. Forensic Glass Analysis by LA-ICP-MS: Assessing the Feasibility of Correlating Windshield Composition and Supplier. *Director* (2010).

14. Sjastad, K.-E., Simonsen, S. L. & Andersen, T. Studies of SRM NIST glasses by laser ablation multicollector inductively coupled plasma source mass spectrometry (LA-ICP-MS). *J. Anal. At. Spectrom.* **27**, 989–999 (2012).
15. Welsch, A.-M., Behrens, H., Horn, I., Roß, S. & Heitjans, P. Self-Diffusion of Lithium in LiAlSi(2)O(6) Glasses Studied Using Mass Spectrometry. *J. Phys. Chem. A* **116**, 309–318 (2012).
16. Van Malderen, S. J. M., van Elteren, J. T. & Vanhaecke, F. Development of a fast laser ablation-inductively coupled plasma-mass spectrometry cell for sub- μm scanning of layered materials. *J. Anal. At. Spectrom.* **30**, 119–125 (2014).
17. Norman, M. D., Griffinab, W. L., Pearsona, N. J. & O'Reilly, M. O. G. and S. Y. Quantitative analysis of trace element abundances in glasses and minerals: a comparison of laser ablation inductively coupled plasma mass spectrometry, solution inductively coupled plasma mass spectrometry, proton microprobe and electron microprobe data. *J. Anal. At. Spectrom.* **13**, 477–482 (1998).
18. Figg, D. & Kahr, S. M. Elemental Fractionation of Glass Using Laser Ablation Inductively Coupled Plasma Mass Spectrometry. *Appl. Spectrosc.* **51**, 1185–1192 (1997).
19. Pisonero, J., Fernandez, B. & Gunther, D. Critical revision of GD-MS, LA-ICP-MS and SIMS as inorganic mass spectrometric techniques for direct solid analysis. *J. Anal. At. Spectrom.* **24**, 1145–1160 (2009).
20. Becker, J. S. & Tenzler, D. Studies of LA-ICP-MS on quartz glasses at different wavelengths of a Nd:YAG laser. *Fresenius. J. Anal. Chem.* **370**, 637–640 (2001).
21. Knowles, M. R. H. Micro-machining of transparent materials with nano, pico and femtosecond lasers -A review. *AILU Work. Ind. Res. Oppor. laser micro nano Process.* (2007).
22. Hassan Hamad, A. Effects of Different Laser Pulse Regimes (Nanosecond, Picosecond and Femtosecond) on the Ablation of Materials for Production of Nanoparticles in Liquid Solution.
23. Bonse, J., Baudach, S., Krueger, J. & Kautek, W. Femtosecond laser micromachining of technical materials. *Proc. SPIE* **4065**, 161–72 ST-- Femtosecond laser micromachining of (2000).
24. Ubide, T., McKenna, C. A., Chew, D. M. & Kamber, B. S. High-resolution LA-ICP-MS trace element mapping of igneous minerals: In search of magma histories. *Chem. Geol.* **409**, 157–168 (2015).
25. Affatigato, M. *et al.* Studies of oxide glass structure using laser ionization time of flight mass spectrometry. *J. Phys. Condens. Matter* **15**, S2323–S2334 (2003).
26. Pangavhane, S. D. *et al.* Laser desorption ionization time-of-flight mass spectrometry of

- erbium-doped Ga-Ge-Sb-S glasses. *Rapid Commun. Mass Spectrom.* **28**, 1221–1232 (2014).
- 27. EAG Laboratories. Secondary Ion Mass Spectrometry (SIMS).
 - 28. EAG Laboratories. Time-of-Flight Secondary Ion Mass Spectrometry (TOF-SIMS).
 - 29. David W. Mogk. Time-of-Flight Secondary Ion Mass Spectrometry (ToF-SIMS). *Geochemical Instrumentation and Analysis* (2016). Available at: http://serc.carleton.edu/research_education/geochemsheets/techniques/ToF-SIMS.html.
 - 30. Kubicek, M. *et al.* A novel ToF-SIMS operation mode for sub 100 nm lateral resolution: Application and performance. *Appl. Surf. Sci.* **289**, 407–416 (2014).
 - 31. Chen, Y.-J. *Secondary Ion Mass Spectrometry*. (2014).
 - 32. Wang, Z., Jin, K., Zhang, Y., Wang, F. & Zhu, Z. ToF-SIMS depth profiling of insulating samples, interlaced mode or non-interlaced mode? *Surf. Interface Anal.* **46**, 257–260 (2014).
 - 33. Behr, W. M., Thomas, J. B. & Hervig, R. L. Calibrating Ti concentrations in quartz for SIMS determinations using NIST silicate glasses and application to the TitaniQ geothermobarometer. *Am. Mineral.* **96**, 1100–1106 (2011).
 - 34. Douglas, M. A. & Chen, P. J. Quantitative Trace Metal Analysis of Silicon Surfaces by ToF-SIMS. **994**, 984–994 (1998).
 - 35. Hervig, R. L. *et al.* Useful ion yields for Cameca IMS 3f and 6f SIMS: Limits on quantitative analysis. *Chem. Geol.* **227**, 83–99 (2006).
 - 36. Nix, R. 5.5: Secondary Ion Mass Spectrometry. *LibreTexts* (2015). Available at: https://chem.libretexts.org/Core/Physical_and_Theoretical_Chemistry/Surface_Science/5%3A_Surface_Analytical_Techniques/5.5%3A_Secondary_Ion_Mass_Spectrometry.
 - 37. Rocholl, A., Dulski, P. & Raczek, I. New ID-TIMS, ICP-MS and SIMS data on the trace element composition and homogeneity of NIST certified reference material SRM 610-611. *Geostand. Newslett.* **24**, 261–274 (2000).
 - 38. Barbalace, K. L. Periodic Table of Elements Sorted by 1st Ionization Potential (eV). *EnvironmentalChemistry.com* (2017). Available at: <https://environmentalchemistry.com/yogi/periodic/1stionization.html>.
 - 39. Kuznetsov, I. *et al.* Ultrasensivite three dimensional nanoscale chemical imaging. in *2015 IEEE Photonics Conference, IPC 2015* 434–435 (2015). doi:10.1109/IPCon.2015.7323706
 - 40. Kuznetsov, I. *et al.* Volumetric Composition Imaging at the Nanoscale by Soft X-Ray Laser Ablation Mass Spectrometry. in 225–231 (2016). doi:10.1007/978-3-319-19521-6_29

41. ER Bernstein. *Photoelectron Spectroscopy of Energetic Materials and Catalytic Clusters with a 26.5 eV Tabletop Laser*. (2015).
42. Bernstein, E. R. *et al.* Application of Soft X-Ray Lasers to Neutral Cluster Chemistry. in 359–367 (2016). doi:10.1007/978-3-319-19521-6_47
43. Kurosawa, M., Jackson, S. E. & Sueño, S. Trace Element Analysis of NIST SRM 614 and 616 Glass Reference Materials by Laser Ablation Microprobe- Inductively Coupled Plasma-Mass Spectrometry. *Geostand. Geoanalytical Res.* **26**, 75–84 (2002).
44. Riedo, A., Neuland, M., Meyer, S., Tulej, M. & Wurz, P. Coupling of LMS with a fs-laser ablation ion source: elemental and isotope composition measurements. *J. Anal. At. Spectrom.* **28**, 1256 (2013).
45. Jochum, K. P. *et al.* Determination of reference values for NIST SRM 610-617 glasses following ISO guidelines. *Geostand. Geoanalytical Res.* **35**, 397–429 (2011).
46. Wise, S. A. & Watters Jr., R. L. Certificate of Analysis, Standard Reference Material 610. 1–4 (2010). doi:10.1080/00365510410006036
47. Wise, S. A. & Watters Jr., R. L. Certificate of Analysis, Standard Reference Material 612. 1–4 (2010).
48. Wise, S. A. & Watters Jr., R. L. Certificate of Analysis, Standard Reference Material 614. 1–4 (2010).
49. Wise, S. A. & Watters Jr., R. L. Certificate of Analysis, Standard Reference Material 616. 1–4 (2010).
50. Nohl, U. GeoReM. Available at: <http://georem.mpch-mainz.gwdg.de/>.
51. Mayer, K., Wallenius, M. & Ray, I. Nuclear forensics--a methodology providing clues on the origin of illicitly trafficked nuclear materials. *Analyst* **130**, 433–441 (2005).
52. Stanley, F. E., Stalcup, A. M. & Spitz, H. B. A brief introduction to analytical methods in nuclear forensics. *J. Radioanal. Nucl. Chem.* **295**, 1385–1393 (2013).
53. Michael May. Nuclear Forensics. *APS NEWS* Available at: <https://www.aps.org/publications/apsnews/200804/backpage.cfm>.
54. Hedberg, P. M. L. *et al.* Improved particle location and isotopic screening measurements of sub-micron sized particles by Secondary Ion Mass Spectrometry. *J. Anal. At. Spectrom.* **26**, 406 (2011).
55. Wallenius, M. & Mayer, K. Age determination of plutonium material in nuclear forensics by thermal ionisation mass spectrometry. *Fresenius. J. Anal. Chem.* **366**, 234–238 (2000).
56. Lloyd, N. S., Parrish, R. R., Horstwood, M. S. A., Chinery, S. R. N. & Bouman, C. ' Nuclear

Forensic™ application of LA -MC-ICP-MS Thermo Fisher Scientific , Bremen , Germany .
IAEA Safeguards Symp. IAEA--CN--184/39 (2010).

57. Kuroski, H., Chang, D. & Inn, K. G. W. In search of higher sensitivity: Pu isotopic analysis. *J. Radioanal. Nucl. Chem.* **269**, 279–281 (2006).
58. Mueller, P. & Vervoort, J. Thermal Ionization Mass Spectrometry (TIMS). *Geochemical Instrumentation and Analysis* Available at:
http://serc.carleton.edu/research_education/geochemsheets/techniques/TIMS.html.
59. Vanhaecke, F. & Degryse, P. *Isotopic analysis Fundamentals and Applications Using ICP-MS.* (2012).
60. Walczyk, T. TIMS versus multicollector-ICP-MS: Coexistence or struggle for survival? *Anal. Bioanal. Chem.* **378**, 229–231 (2004).
61. Dynamic SIMS. *Big Chemical Encyclopedia* (2015). Available at:
<http://chempedia.info/info/69678/>.
62. Benware, B. R., Macchietto, C. D., Moreno, C. H. & Rocca, J. J. Demonstration of a High Average Power Tabletop Soft X-Ray Laser. *Phys. Rev. Lett.* **81**, 5804–5807 (1998).
63. Heinbuch, S., Grisham, M., Martz, D. & Rocca, J. J. Demonstration of a desk-top size high repetition rate soft x-ray laser. *Opt. Express* **13**, 4050 (2005).
64. Urbanski, L. Coherent Euv Lithography With Table-Top Laser. (2012).
65. Heinbuch, S. DESK-TOP SIZE HIGH REPETITION RATE 46.9 NM CAPILLARY DISCHARGE LASER AS PHOTOIONIZATION SOURCE FOR PHOTOCHEMISTRY APPLICATIONS. (2006).
66. Kuznetsov, I. *Design and operation characteristics of a high repetition rate desk-top size 46.9 nm capillary discharge laser.*
67. Neuhoff, J. Certificate of Analysis CRM U200. 68521–68521 (2008).
doi:10.1080/00365510410006036
68. Passarelli, M. K. *et al.* Development of an Organic Lateral Resolution Test Device for Imaging Mass Spectrometry. *Anal. Chem.* **86**, 9473–9480 (2014).
69. B.L. Henke, E.M. Gullikson, and J. C. D. X-ray interactions: photoabsorption, scattering, transmission, and reflection at E=50-30000 eV, Z=1-92. *At. Data Nucl. Data Tables* **54**, 181–342 (1993).
70. Sigmund, P. Theory of sputtering. I. Sputtering yield of amorphous and polycrystalline targets. *Phys. Rev.* **184**, 383–416 (1969).
71. EAG Laboratories. Analytical Resolution versus Detection Limit Typical Analysis Depths for Techniques. (2013).